Eur. Phys. J. B (2015)
DOI: 10.1140/epjb/e2015-60468-7

THE EUROPEAN PHYSICAL JOURNAL B

Regular Article

Continuum modeling of particle redeposition during ion-beam erosion

Laterally two-dimensional case

Christian Diddens[1,a] and Stefan J. Linz[2,b]

[1] Department of Mechanical Engineering, Eindhoven University of Technology, P.O. Box 513, 5600 MB Eindhoven, The Netherlands
[2] Institut für Theoretische Physik, Universität Münster, 48149 Münster, Germany

Received 12 June 2015
Published online (Inserted Later)

Abstract. We thoroughly investigate the impact of redeposition on the self-organized pattern formation during ion-beam erosion within the framework of a spatially two-dimensional continuum model. An analysis on prestructured patterns allows the extraction of general properties of this mechanism, the typical distribution of redepositing particles and approximations in terms of the surface height in particular. By combining the redeposition model with erosion models, we present detailed results about the impact of redeposition on spatio-temporal surface evolutions. It is shown that redeposition can play a decisive role for pattern formation under ion-beam erosion within an extended range in the parameter space.

1 Introduction

Self-organized pattern formation is ubiquitous in nature and can be observed on length scales ranging from the macro- to the nanoscale. For application, in particular the latter is relevant: when the desired length scale is below the range of conventional top-down methods, e.g. lithographic microfabrication, self-organized pattern formation provides a promising bottom-up alternative to create structures on the nanoscale [1].

One prime example for this approach is the emergence of well-structured morphologies on ion-beam eroded surfaces (cf. Refs. [1–4] for reviews). While the first experiments can be dated back to 1962 [5], a new impetus was given in 1999, when Facsko et al. discovered the self-organized formation of hexagonally arranged nanodot structures on semiconductor surfaces by low-energy ion-beam erosion at normal incidence [6]. Since then, numerous experiments have been carried out which can essentially be categorized into three groups: (i) low-energy erosion of III-V semiconductor compounds [6–11]; (ii) erosion of Ge with heavy ions or ion clusters [12–17] and (iii) low-energy erosion of Si with additional metal co-deposition [18–21].

From the theoretical point of view, continuum models offer a promising approach to gain a coarse-grained understanding of the physical mechanisms acting on the eroded surface and their interplay leading to the observed nanopatterns. By expanding the evolution $\partial_t H$ of the surface height $H(\mathbf{x},t)$ (with the lateral coordinate $\mathbf{x}=(x,y)$) into lowest order terms that are compatible with the symmetry, Cuerno and Barabási proposed an isotropic Kuramoto-Sivashinsky (KSE) equation as minimal model for normal ion-incidence [22]:

$$\partial_t H = a_0 + a_1\nabla^2 H + a_2\nabla^4 H + a_3\left(\nabla H\right)^2. \qquad (1)$$

Here, the individual terms on the rhs can be interpreted as follows: while $a_0<0$ is the erosion velocity of a completely flat surface, $a_2\nabla^4 H$ (with $a_2<0$) represents the smoothing Mullins diffusion [23] and $a_3\left(\nabla H\right)^2$ models the tilt-dependence of the sputter yield to the lowest order. The coefficient a_1 of the (anti)diffusive term $\nabla^2 H$ has a positive, i.e. smoothing, contribution stemming from the ballistic mass drift [24] but must also comprise roughening mechanisms that lead to a in total negative a_1 so that an initially flat surface is destabilized in the model equation (1). The Bradley-Harper mechanism, i.e. the curvature-dependence of the erosion rate [25], gives rise to a term proportional to $-\nabla^2 H$, but also chemical roughening mechanisms have been proposed [26]. For the afore-mentioned case (iii), the deflection of approaching metal atoms constitutes a reasonable roughening mechanism since it has be successfully identified in the field of physical vapor deposition of a thin metallic film on Si [27–29].

However, it is well-known that the generic solutions of the Kuramoto-Sivashinsky equation are spatio-temporal chaotic [30,31] and, hence, the model (1) cannot account

[a] e-mail: C.Diddens@tue.nl
[b] e-mail: slinz@wwu.de

for the observed self-organized pattern formation. To that end, a variety of generalizations of equation (1) have been proposed and investigated [32–43]. The outcome can be concluded as follows: in order to reproduce hexagonally arranged dots with a generalized Kuramoto-Sivashinsky equation, one either has to incorporate a non-local term or couple in an additional surface composition equation [36,37]. For the first case, the most simple non-locality is a linear damping term proportional to the relative surface height $H-\bar{H}$, where $\bar{H}(t)$ is the surface mean height, i.e. the spatial height average. Facsko et al. proposed the inclusion of a linear damping term $b(H-\bar{H})$ with $b<0$ and attributed its physical origin to redeposition, i.e. the reattachment of previously eroded target particles [33].

While redeposition has been investigated in detail in the field of focused ion-beam milling [44–48], its impact on the self-organized pattern formation during ion-beam erosion has been controversially discussed: Anspach and Linz concluded based on the results of a discrete solid-on-solid model that redeposition shares substantial properties with the damping term [49]. For a more exact model, however, one has to incorporate higher order terms, in particular a quadratic damping term $c(H-\bar{H})^2$, and the coefficients depend on the aspect ratio of the morphology [50]. In contrast, Bradley argued on the basis of a continuum model valid for small height gradients that redeposition cannot give rise to a linear damping term and, therefore, cannot account for the formation of hexagonally ordered patterns [51].

In our previous publications, we have performed a detailed analysis of a one-dimensional variant of a continuum model for redeposition [52], which contains the model of Bradley as a limit, and discussed first results of the corresponding two-dimensional model [53]. We were able to clarify that redeposition in fact sets in quadratically for very flat surfaces, but – with increasing roughness – a linear damping term and higher order terms with coefficients depending on the aspect ratio set in. Most importantly, we were able to show that the undamped Kuramoto-Sivashinsky equation (1) in combination with the redeposition model is able to reproduce well-ordered structures in both one and two dimensions.

The aim of this study is the pending detailed investigation of the physical realistic two-dimensional continuum model for redeposition that is not confined to small height gradients. Since this article is quite comprehensive, we outline its contents in the following: in Section 2 the model is derived and the ingredients and basic properties are presented. By considering limiting cases, we additionally show the connection of our generalized two-dimensional model to the small-gradient approximation by Bradley [51] and to our one-dimensional variant [52], respectively.

Subsequently, the effect of pure redeposition on pre-structured surfaces is analyzed in Section 3. Focusing on hexagonally ordered patterns, the influence of the sputter yield and the angular erosion distribution is discussed in detail. In particular, we demonstrate that the complicated redeposition model can be approximated by rather simple, in general non-local, terms of the surface height.

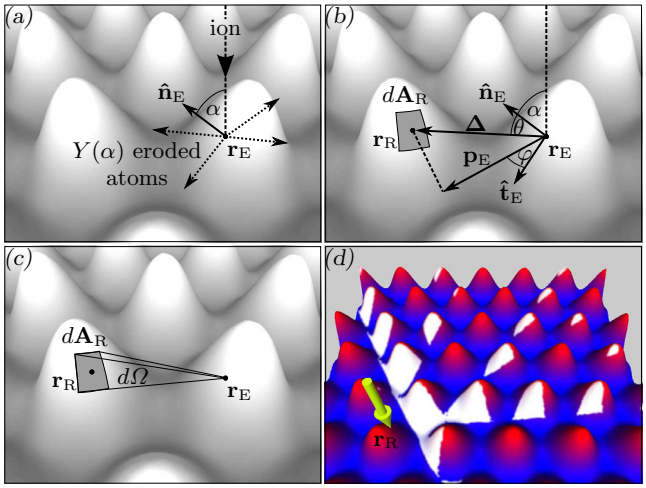

Fig. 1. Derivation of the continuum model for redeposition: (a) an ion hits the surface at $\mathbf{r}_\mathrm{E}$ and erodes $Y(\alpha)$ particles. (b) Definition of the local spherical coordinates (θ,φ). (c) Calculation of the number of redepositing particles by integrating $Y(\alpha)f(\alpha,\theta,\varphi)$ over $d\Omega$. (d) Integration over all visible surface areas (white regions).

In Section 4 the redeposition model is finally coupled with erosion models and the spatio-temporal interplay of both processes is thoroughly investigated. Substantiated by a parameter map and by taking a variety of model combinations into account, we conclude that redeposition can be a decisive and robust trigger for the emerge of self-organized pattern formation. Contrary to the argumentation of Bradley [51], this also holds true for the small-gradient approximation of redeposition.

In Appendix A, the novel elaborate numerical technique to simulate redeposition on reasonable time scales is given.

2 Continuum model for redeposition

2.1 Derivation

We start our derivation by separating the spatio-temporal evolution of the surface height $H(\mathbf{x},t)$ with $\mathbf{x}=(x,y)$ into two contributions:

$$\partial_t H = F_\mathrm{R}[H] + F_\mathrm{E}[H]. \tag{2}$$

Here, the functional F_R describes the height growth due to pure redeposition, whereas F_E comprises all effects that are caused by erosion and diffusion. Since we are interested in the impact of pure redeposition for the moment, we temporarily set $F_\mathrm{E}=0$. The following derivation of our redeposition model F_R is illustrated in Figure 1. Our model is a generalization of previous works by Smith et al. [44,45] and Bradley [51].

In order to obtain the height growth velocity due to pure redeposition F_R, one is interested in the number of eroded particles that redeposit on an infinitesimal surface element $d\mathbf{A}_\mathrm{R}$ at $\mathbf{r}_\mathrm{R}=(\mathbf{x}_\mathrm{R},H_\mathrm{R})$ with $H_\mathrm{R}=H(\mathbf{x}_\mathrm{R},t)$ per time. When an ion hits the surface at another position

$\mathbf{r}_\mathrm{E} = (\mathbf{x}_\mathrm{E}, H_\mathrm{E})$ with $H_\mathrm{E} = H(\mathbf{x}_\mathrm{E}, t)$, the average number of eroded particles is given by the sputter yield $Y(\alpha)$, where

$$\alpha = \arccos \frac{1}{\sqrt{1 + (\nabla H_\mathrm{E})^2}} \tag{3}$$

is the local angle of incidence. For the moment, we neglect the Bradley-Harper effect, i.e. a dependence of Y on the surface curvature. This influence is investigated later on in Section 3.5.2. Since the eroded atoms do not leave the surface isotropically, we introduce the angular erosion distribution $f(\alpha, \theta, \varphi)$ to model preferential erosion directions. The latter distribution is a function of the angle of incidence α and of two erosion angles θ and φ which are defined by a local spherical coordinate system at $\mathbf{r}_\mathrm{E}$. The polar angle $\theta \in [0, \pi/2)$ is defined with respect to the surface normal

$$\hat{\mathbf{n}}_\mathrm{E} = \frac{-\nabla H_\mathrm{E} + \hat{\mathbf{e}}_H}{\sqrt{1 + (\nabla H_\mathrm{E})^2}}, \tag{4}$$

whereas the azimuthal angle $\varphi \in [-\pi, \pi]$ is zero if the erosion direction coincides with the positive quadrant of the plane spanned by $\hat{\mathbf{n}}_\mathrm{E}$ and the downhill tangent

$$\hat{\mathbf{t}}_\mathrm{E} = -\frac{\nabla H_\mathrm{E} + (\nabla H_\mathrm{E})^2 \cdot \hat{\mathbf{e}}_H}{\sqrt{(\nabla H_\mathrm{E})^2 + (\nabla H_\mathrm{E})^4}}. \tag{5}$$

In the case of locally normal incidence, i.e. $\alpha = 0$, the tangent $\hat{\mathbf{t}}_\mathrm{E}$ and thereby the angle φ cannot be defined. However, f has to be independent of φ under this circumstances. Since the total number of eroded particles is already given by the sputter yield $Y(\alpha)$, the function $f(\alpha, \theta, \varphi)$ has to be normalized, i.e.

$$\int_0^{\pi/2} d\theta \int_{-\pi}^{\pi} d\varphi \, \sin\theta \, f(\alpha, \theta, \varphi) = 1 \tag{6}$$

has to hold for all $\alpha \in [0, \pi/2)$.

The average number of atoms that are eroded by the ion impact at $\mathbf{r}_\mathrm{E}$ and redeposit on the surface element $d\mathbf{A}_\mathrm{R}$ at $\mathbf{r}_\mathrm{R}$ can be calculated by the integration of $Y(\alpha) f(\alpha, \theta, \varphi)$ over the solid angle $d\Omega$ that encloses the area $d\mathbf{A}_\mathrm{R}$ with the vertex $\mathbf{r}_\mathrm{E}$. Within this infinitesimal integration, the erosion angles θ and φ are given by:

$$\cos\theta = \frac{\hat{\mathbf{n}}_\mathrm{E} \cdot \boldsymbol{\Delta}}{\|\boldsymbol{\Delta}\|} = \frac{\Delta H - \Delta\mathbf{x} \cdot \nabla H_\mathrm{E}}{\sqrt{\left[1 + (\nabla H_\mathrm{E})^2\right] \cdot \left[(\Delta\mathbf{x})^2 + (\Delta H)^2\right]}} \tag{7}$$

and

$$\cos\varphi = \frac{\mathbf{p}_\mathrm{E} \cdot \hat{\mathbf{t}}_\mathrm{E}}{\|\mathbf{p}_\mathrm{E}\|}, \tag{8}$$

where $\Delta\mathbf{x} = \mathbf{x}_\mathrm{R} - \mathbf{x}_\mathrm{E}$, $\Delta H = H_\mathrm{R} - H_\mathrm{E}$ and $\mathbf{p}_\mathrm{E} = \boldsymbol{\Delta} - (\hat{\mathbf{n}}_\mathrm{E} \cdot \boldsymbol{\Delta}) \hat{\mathbf{n}}_\mathrm{E}$ denotes the projection of the direction vector $\boldsymbol{\Delta} = (\Delta\mathbf{x}, \Delta H)$ onto the tangential plane of the surface at $\mathbf{r}_\mathrm{E}$. With $d\mathbf{A}_\mathrm{R} = (-\nabla H_\mathrm{R} + \hat{\mathbf{e}}_H) d^2 x_\mathrm{R}$ the solid angle can be written as:

$$d\Omega = -\frac{\boldsymbol{\Delta} \cdot d\mathbf{A}_\mathrm{R}}{\|\boldsymbol{\Delta}\|^3} = -\frac{\Delta H - \Delta\mathbf{x} \cdot \nabla H_\mathrm{R}}{\left[(\Delta\mathbf{x})^2 + (\Delta H)^2\right]^{3/2}} \, d^2 x_\mathrm{R}. \tag{9}$$

However, the erosion event at $\mathbf{r}_\mathrm{E}$ can only contribute to the redeposition at $\mathbf{r}_\mathrm{R}$ if the connecting line between these points is not obstructed by other parts of the surface. To that end, we introduce the indicator function $v_H(\mathbf{x}_\mathrm{R}, \mathbf{x}_\mathrm{E})$ for the visibility of both points, i.e. $v_H(\mathbf{x}_\mathrm{R}, \mathbf{x}_\mathrm{E})$ yields 1 if the points are visible with respect to the surface and 0 if the connecting line is obstructed by surface parts lying in between. Thus, the number of particles eroded by the impinging ion at $\mathbf{r}_\mathrm{E}$ that redeposit at the surface element $d\mathbf{A}_\mathrm{R}$ at $\mathbf{r}_\mathrm{R}$ is given by:

$$v_H(\mathbf{x}_\mathrm{R}, \mathbf{x}_\mathrm{E}) Y(\alpha) f(\alpha, \theta, \varphi) \frac{\Delta\mathbf{x} \cdot \nabla H_\mathrm{R} - \Delta H}{\left[(\Delta\mathbf{x})^2 + (\Delta H)^2\right]^{3/2}} d^2 x_\mathrm{R}, \tag{10}$$

whereby the angles α, θ and φ have to be evaluated according to equations (3), (7) and (8).

The last step in the derivation of our model is the generalization of the single ion impact at $\mathbf{r}_\mathrm{E}$ to a homogeneous irradiation of the whole surface with a constant ion flux J (i.e. number of impinging ions per area and time). This is achieved by taking the surface integral $J \int d^2 x_\mathrm{E}$ of equation (10). The height growth velocity due to pure redeposition F_R is finally given by the multiplication with the volume of a target atom V_a:

$$F_\mathrm{R}(\mathbf{x}_\mathrm{R}, t) = V_\mathrm{a} J \int v_H(\mathbf{x}_\mathrm{R}, \mathbf{x}_\mathrm{E}) Y(\alpha) f(\alpha, \theta, \varphi) \times \frac{\Delta\mathbf{x} \cdot \nabla H_\mathrm{R} - \Delta H}{\left[(\Delta\mathbf{x})^2 + (\Delta H)^2\right]^{3/2}} \, d^2 x_\mathrm{E}. \tag{11}$$

The non-local surface integral (11) constitutes the general form of our redeposition model which is valid for arbitrary surface morphologies. In the remainder of this article, we will analyze F_R in detail.

2.2 Model properties

In the following, the intrinsic properties of the redeposition functional (11) are discussed. We address assumptions made in the derivation, invariances and symmetries as well as specific limits and the relation to our one-dimensional redeposition model [52].

2.2.1 Assumptions

In the derivation, we have implicitly assumed a sticking coefficient of unity, i.e. that each impinging, previously eroded particle redeposits on the surface. A stick-or-leave scenario, i.e. the particle either sticks to it with a given probability or leaves the surface into the vacuum in the other case, with a constant sticking coefficient less than 1 can be modeled by multiplying the rhs of (11) with the latter factor. Within the evolution equation for pure redeposition, $\partial_t H = F_\mathrm{R}$, this corresponds to a rescaling of time. Although it is basically feasible to generalize our model to more complicated scenarios, e.g. possibly multiple bounces before the actual redeposition event, it comes at the cost of a vast increase of complexity. However, in the framework of the SOS-model it was shown that these generalizations do not influence the redeposition mechanism

in a qualitative manner [49]. This result substantiates our simplification.

Additionally, it was assumed that the time of flight between an erosion and a redeposition event can be considered as instantaneously with respect to the surface evolution velocity $\partial_t H$.

2.2.2 The visibility function v_H

In the surface integral (11), there is an additional nonlocality within the visibility function $v_H(\mathbf{x}_\mathrm{R}, \mathbf{x}_\mathrm{E})$. With the definition of the height difference

$$d_H(\mathbf{x}_\mathrm{R}, \mathbf{x}_\mathrm{E}, \mu) = \mu \Delta H + H_\mathrm{E} - H((1-\mu)\cdot\mathbf{x}_\mathrm{E} + \mu\cdot\mathbf{x}_\mathrm{R}, t) \tag{12}$$

between the connecting line of $\mathbf{r}_\mathrm{E}$ and $\mathbf{r}_\mathrm{R}$ and the surface height beneath, the visibility function can be formally defined by:

$$v_H(\mathbf{x}_\mathrm{R}, \mathbf{x}_\mathrm{E}) = \begin{cases} 1 \text{ if } d_H(\mathbf{x}_\mathrm{R}, \mathbf{x}_\mathrm{E}, \mu) \geq 0 \text{ for all } \mu \in [0,\,1] \\ 0 \qquad\qquad\qquad \text{otherwise.} \end{cases} \tag{13}$$

As it can be seen, v_H is symmetric, i.e. $v_H(\mathbf{x}_\mathrm{R}, \mathbf{x}_\mathrm{E}) = v_H(\mathbf{x}_\mathrm{E}, \mathbf{x}_\mathrm{R})$ holds for all $\mathbf{x}_\mathrm{R}$ and $\mathbf{x}_\mathrm{E}$. This fact is exploited in the numerical algorithm (cf. Appendix A). Furthermore, d_H and thereby v_H are invariant under invertible affine transformations of the lateral coordinate system $\mathbf{x}$. In particular, a lateral scaling $\mathbf{x} \to s_x\mathbf{x}$ of the surface preserves the visibility. The same holds also true for a scaling $H \to s_H H$ of the height dimension, however, with the restriction $s_H > 0$. For $s_H < 0$, d_H changes the sign and, therefore, all previously visible pairs $(\mathbf{x}_\mathrm{R}, \mathbf{x}_\mathrm{E})$ become invisible, whereas pairs which connecting lines previously run entirely below the surface turn visible after the transformation.

2.2.3 Scale invariance

An inherent property of the redeposition model (11) is the scale invariance with respect to an aspect ratio conserving, isotropic scaling of the height and lateral extents, i.e.

$$\{\mathbf{x} \to s\mathbf{x}, H \to sH\} \quad \text{with} \quad s > 0. \tag{14}$$

The angular quantities α, θ and φ are preserved, whereas the scaling $d\Omega \to s^{-2} d\Omega$ is canceled out by the integral $\int d^2x_\mathrm{E} \to s^2 \int d^2x_\mathrm{E}$. As a result, the same redeposition F_R acts on a small-scale surface as on the isotropically scaled up equivalent. Within the spatio-temporal evolution equation for pure redeposition, $\partial_t H = F_\mathrm{R}$, the time t has to be scaled by $t \to st$ to absorb the scaling factor in the lhs. Thus, the small-scale surface evolves *relatively* faster than the corresponding large-scale one due to the same *absolute* redeposition effect. In the SOS-model, the same scale invariance can be extracted from the numerical results [50].

On the one hand, the scale invariance simplifies the analysis of the redeposition effect since, for a given morphology, F_R does not directly depend on the surface amplitude A and on the characteristic lateral length L (i.e. dot-to-dot distance), but only on the aspect ratio

$$\epsilon = \frac{A}{L}. \tag{15}$$

In order to absorb intrinsic height and lateral scales, we introduce the normalized spatial coordinate $\hat{\mathbf{x}}$ and the normalized relative height $\hat{h}$:

$$\hat{\mathbf{x}} = \frac{\mathbf{x}}{L}, \qquad \hat{h} = \frac{H - \bar{H}}{A}. \tag{16}$$

On the other hand, the scale invariance constrains surmisable approximations of the redeposition mechanism. In particular, considering a nearly flat surface with a small relative height $h = H - \bar{H} \approx 0$, one is interested in a linear approximation of F_R, i.e.

$$F_\mathrm{R} = \sum_{n=0} c_{2n} \nabla^{2n} h + \text{nonlinear terms}. \tag{17}$$

For constant coefficients c_{2n}, this approximation can only fulfill the scale invariance if $c_{2n} = 0$ for all n. Thus, F_R cannot have a universally valid linear portion with constant coefficients. In contrast, there are nonlinear terms like $(\nabla h)^2$, $h\nabla^2 h$, ... that are compatible with the scale invariance. However, as we have already shown in the investigation of the one-dimensional variant of the redeposition model, an accurate approximation requires the inclusion of a linear damping term proportional to h with a coefficient depending on the aspect ratio [52]. We will address this statement over the course of this article.

The scale invariance is violated by the dependence on the surface curvature when the Bradley-Harper effect is taken into account. We investigate its influence on the redeposition mechanism later on in Section 3.5.2.

2.2.4 Small-gradient approximation

If the aspect ratio ϵ is small, we can approximate F_R for small height gradients. Due to the scale invariance, we can scale the surface to have a characteristic length $L = 1$ followed by a Taylor expansion for small amplitudes $A \approx 0$. In this limit, $\alpha \approx 0$ and $\theta \approx \pi/2$ holds. Using the symmetry requirements $\partial_\alpha Y(\alpha = 0) = 0$ and $\partial_\varphi f(\alpha = 0, \theta, \varphi) = 0$, one obtains up to the quadratic order in A:

$$F_\mathrm{R} \approx J\, V_\mathrm{a}\, Y(0) \int d^2x_\mathrm{E}\, v_H(\mathbf{x}_\mathrm{R}, \mathbf{x}_\mathrm{E})\, \frac{\Delta\mathbf{x}\cdot\nabla\hat{h}_\mathrm{R} - \Delta\hat{h}}{\|\Delta\mathbf{x}\|^3} \times \left[f_0 \cdot A + \left(f_\alpha \|\nabla\hat{h}_\mathrm{E}\| + f_\theta \frac{\Delta\hat{h} - \Delta\mathbf{x}\cdot\nabla\hat{h}_\mathrm{E}}{\|\Delta\mathbf{x}\|} \right) \cdot A^2 \right]. \tag{18}$$

Here, $\hat{h}_\mathrm{R}$, $\hat{h}_\mathrm{E}$ and $\Delta\hat{h}$ correspond to H_R, H_E and ΔH normalized by the amplitude A. The erosion distribution

in tangential direction $f_0 = f(\alpha = 0, \theta = \pi/2, \varphi)$ and its increase $f_\theta = -\partial_\theta f(\alpha = 0, \theta = \pi/2, \varphi)$ for decreasing θ are independent of φ, whereas $f_\alpha = \partial_\alpha f(\alpha = 0, \theta = \pi/2, \varphi)$ has to be evaluated at

$$\varphi \approx \arccos\left(-\frac{\Delta\mathbf{x}\cdot\nabla\hat{h}_\mathrm{E}}{\|\Delta\mathbf{x}\|\cdot\|\nabla\hat{h}_\mathrm{E}\|}\right). \tag{19}$$

Keeping in mind the scale invariance, one can read off from equation (18) that a linear increase of F_R with the aspect ratio $\epsilon \approx 0$ can only be expected if $f_0 > 0$, i.e. if particles eroded at normal incidence can leave the surface tangentially. In the case $f_0 = f_\alpha = 0$, equation (18) becomes the small-gradient redeposition model proposed by Bradley [51]:

$$F_\mathrm{R}^\mathrm{B} = J\, V_\mathrm{a}\, Y(0)\, f_\theta \int d^2x_\mathrm{E}\, v_H(\mathbf{x}_\mathrm{R}, \mathbf{x}_\mathrm{E}) \times \frac{[\Delta\mathbf{x}\cdot\nabla H_\mathrm{R} - \Delta H]\cdot[\Delta H - \Delta\mathbf{x}\cdot\nabla H_\mathrm{E}]}{\|\Delta\mathbf{x}\|^4}. \tag{20}$$

2.3 Models for Y and f

In the following, we address the models we have used for the sputter yield $Y(\alpha)$ and the angular erosion distribution $f(\alpha, \theta, \varphi)$. In order to get insight in the influence of the specific choice of these, we have investigated a variety of models, ranging from most simple to physical realistic variants.

2.3.1 Sputter yield Y(α)

To temporarily neglect the influence of the tilt-dependent sputter yield, $Y(\alpha)$ can be considered as constant, i.e.

$$Y(\alpha) = Y_\mathrm{const} = 1, \tag{21}$$

where the particular value of Y_const can be changed by rescaling the resulting F_R. In view of equations (18) and (20), this model remains valid at least at small aspect ratios. When the aspect ratio increases, the tilt-dependence of $Y(\alpha)$ can influence the redeposition effect F_R. To that end, we have used a model proposed by Wei et al., which is in good agreement with the experimental data for the sputter yield [54]:

$$Y(\alpha) = Y_\mathrm{tilt}(\alpha) = Y_0 \cos(\alpha) \exp\left(\frac{\sin^2(\alpha)}{2\cos^2(\alpha_\mathrm{max})}\right). \tag{22}$$

According to experiments [55], we have used the angle of maximum erosion $\alpha_\mathrm{max} = 65°$, while

$$Y_0 = \frac{\sqrt{\pi}}{\sqrt{2}\,\mathrm{erfi}\left(\frac{1}{\sqrt{2}\cos(\alpha_\mathrm{max})}\right)\cos(\alpha_\mathrm{max})} \approx 0.4210585834, \tag{23}$$

was chosen in order to have the same mean value of Y_const and $Y_\mathrm{tilt}(\alpha)$ with respect to α.

As already stated, we investigate the influence of the Bradley-Harper effect separately in Section 3.5.2.

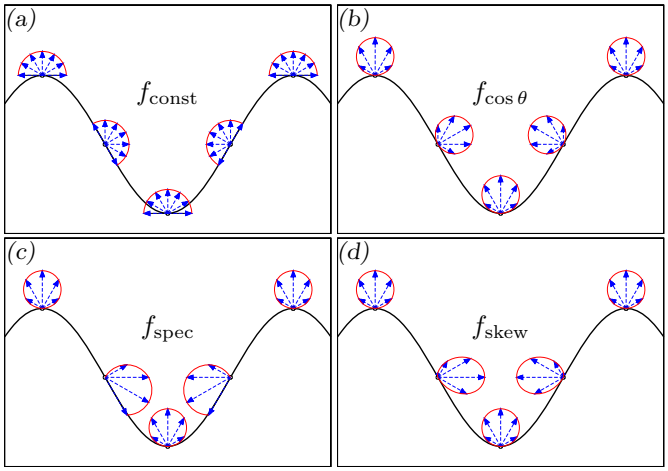

Fig. 2. Different models for the angular erosion distribution f. The length of the arrows indicate the number of particles leaving the surface in the indicated direction.

2.3.2 Angular erosion distribution f(α, θ, φ)

Similar to Y_const, the most simple model for f is the uniform distribution

$$f(\alpha, \theta, \varphi) = f_\mathrm{const} = \frac{1}{2\pi}. \tag{24}$$

The factor $1/(2\pi)$ ensures the normalization (cf. Eq. (6)). f_const leads to an isotropic erosion of particles, in particular with a non-vanishing contribution in tangential direction (cf. Fig. 2a).

A physically more realistic model is a cosine-distribution centered around the local surface normal $\hat{\mathbf{n}}_\mathrm{E}$ (cf. Fig. 2b):

$$f(\alpha, \theta, \varphi) = f_{\cos\theta}(\theta) = \frac{\cos\theta}{\pi}. \tag{25}$$

This model can be considered as an average of the experimentally observed under- and over-cosine distributions, i.e. $f \propto (\cos\theta)^p$ with $p < 1$ or $p > 1$ [56,57], respectively. However, for an ion-impact at a slope, $\alpha \neq 0$, the maximum of f can be tilted in downhill direction [58]. This fact can be taken into account by considering a cosine-distribution centered around the direction of specular reflection of the ion-beam on the surface:

$$f(\alpha, \theta, \varphi) = f_\mathrm{spec}(\alpha, \theta, \varphi) = \frac{2}{\pi\cdot(1+\cos\alpha)} \times \max\left(\cos\alpha\cos\theta + \sin\alpha\sin\theta\cos\varphi,\, 0\right). \tag{26}$$

For $\alpha > 0$, f_spec has a non-vanishing erosion distribution in grazing direction (cf. Fig. 2c). The properties $f(\alpha, \theta = \pi/2, \varphi) = 0$ of $f_{\cos\theta}$ and the enhanced downhill contribution of f_spec for $\alpha > 0$ can be combined in a fourth, probably most physically realistic model

$$f(\alpha, \theta, \varphi) = f_\mathrm{skew}(\alpha, \theta, \varphi) = \frac{\cos\theta}{\pi}\left(1 + \cos\varphi\sin\theta\sin\alpha\right). \tag{27}$$

f_{skew} constitutes a cosine-distribution centered around the normal $\hat{\mathbf{n}}_{\text{E}}$ which is additionally skewed in downhill direction (cf. Fig. 2d).

In the following, all four model variants of f are considered. Thereby, we are able to determine the influence of the angular erosion distribution on the redeposition mechanism. With reference to equation (18), we note that $f_0 = 1/(2\pi) \neq 0$ and $f_\alpha = f_\theta = 0$ holds for f_{const}. Thus, a linear onset of F_{R} with the aspect ratio $\epsilon = A/L$ can be expected. Contrarily, $f_0 = 0$ and $f_\theta = 1/\pi \neq 0$ holds for the other models of f and, therefore, F_{R} quadratically sets in with ϵ. The small-gradient approximation by Bradley (20), however, can only be used for $f_{\cos\theta}$ and f_{skew} since f_{spec} does not meet the requirement $f_\alpha = 0$.

2.4 Connection to the one-dimensional variant

In our previous work [52], we have studied a one-dimensional variant of the redeposition model (11) in detail. In the following we show that the one-dimensional variant is actually a special case that can be directly derived from the two-dimensional model. By considering a surface with a translation invariance in y-direction, i.e. a morphology which is infinitely extended in y-direction and fulfilling $H(x, y, t) = H(x, t)$, the y_{E}-integral can be carried out. While the incidence angle α and the visibility function v_H do not depend on y_{E}, the integral of the two-dimensional angular distribution $f(\alpha, \theta, \varphi)$ has to be calculated depending on the specific model. For f_{const}, $f_{\cos\theta}$ and f_{spec} the y_{E}-integration yields exactly the corresponding one-dimensional variant as given in reference [52] for F_{R}. In the case f_{skew}, however, the corresponding one-dimensional angular distribution reads

$$f^{\text{1d}}(\alpha, \theta_{\text{1d}}) = \frac{\cos\theta_{\text{1d}}}{2}\left(1 + \frac{8}{3\pi}\sin\alpha\sin\theta_{\text{1d}}\right), \tag{28}$$

which is slightly less tilted in downhill direction in comparison to the model for $f^{\text{1d}}_{\text{skew}}$ investigated in our one-dimensional article [52].

Since the one-dimensional variant of F_{R} can be considered as a limiting case of the two-dimensional model, all findings discussed in our article [52] can also be interpreted as the results stemming from physically realistic two-dimensional surfaces.

3 Redeposition on static surfaces

We start our analysis of the redeposition model F_{R} by focusing on pre-patterned, static surfaces. We are interested in how redeposition is distributed on different morphologies, especially hexagonally arranged dot and hole patterns. Due to the complexity of the redeposition model and the entering visibility function in particular, it is unlikely to find analytical solutions[1] or even approximations for F_{R}. Therefore, one is confined to numerical calculations. An outline of the numerical algorithm is given in Appendix A.

The morphologies we investigate are given by:

$$H(x, y) = \pm\frac{2A}{9}\left(\cos(kx) + 2\cos\left(\frac{kx}{2}\right)\cos\left(\frac{\sqrt{3}ky}{2}\right)\right), \tag{29}$$

which corresponds to a perfectly hexagonally arranged array of dots (+) and holes (−), respectively. The difference between maximum and minimum height is given by the amplitude A, whereas the characteristic lateral length L, i.e. the dot-to-dot distance, enters equation (29) by the relation $L = 4\pi/(\sqrt{3}k)$. As already discussed in Section 2.2.2, the values of the visibility function v_H cannot be transferred from dots to holes or vice versa. Therefore, both morphologies have to be treated separately. Furthermore, we start our analysis with the constant model Y_{const} for the sputter yield and investigate the impact of the tilt- and curvature-dependent sputter yield later on in Section 3.5.

3.1 Redeposition ratio

An interesting quantity is the redeposition ratio

$$\eta = \frac{N_{\text{R}}}{N_{\text{E}}}, \tag{30}$$

where

$$N_{\text{E}} = J\int d^2x_{\text{E}}\, Y(\alpha) \tag{31}$$

is the total number of eroded atoms per time and

$$N_{\text{R}} = \frac{1}{V_{\text{a}}}\int d^2x_{\text{R}}\, F_{\text{R}}(\mathbf{x}_{\text{R}}) \tag{32}$$

represents the total number of redepositing particles per time. We start our investigation of the redeposition mechanism with the ratio η since, being independent from $\mathbf{x}$, it is the most simple quantity. η only depends on the aspect ratio ϵ, the morphology (dots/holes) and the specific models for the sputter yield Y and the angular erosion distribution f. The redeposition ratio η as function of ϵ is shown for the different morphologies and models for f in Figure 3. As it was expected with a glance at (18), the fraction of redepositing particles sets in with ϵ^2 for all f-models except for f_{const}. For the latter a linear increase of η with ϵ can be found. In the limit of high aspect ratios the redeposition ratio η asymptotically converges to unity since only particles eroded into straight upward directions can entirely leave the surface. Due to the pronounced erosion probability towards the valleys, the angular erosion models f_{spec} and f_{skew} shows higher redeposition ratios η in this limit. For dots with an aspect ratio of unity, corresponding to typical extents of experimental findings on GaSb [6] and Ge [13], more than 50% of all eroded particles reattaches to the surface again. Since we have assumed

[1] In the light of Section 2.4 the two analytical solutions from our one-dimensional investigation [52] can be transferred to the two-dimensional model.

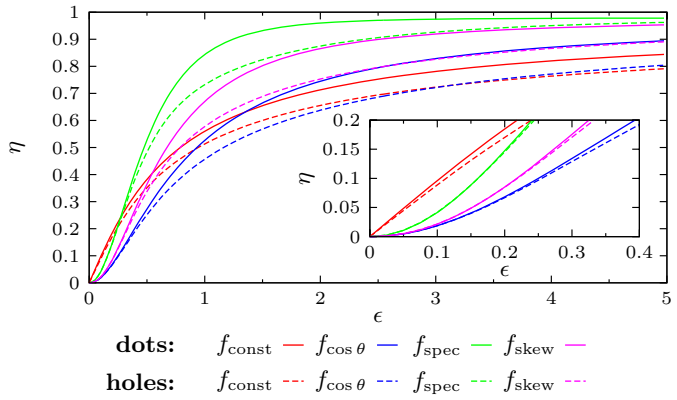

Fig. 3. Redeposition ratio F_{R} as function of the aspect ratio ϵ for the hexagonally arranged dots and holes and for the different models for f and Y_{const}.

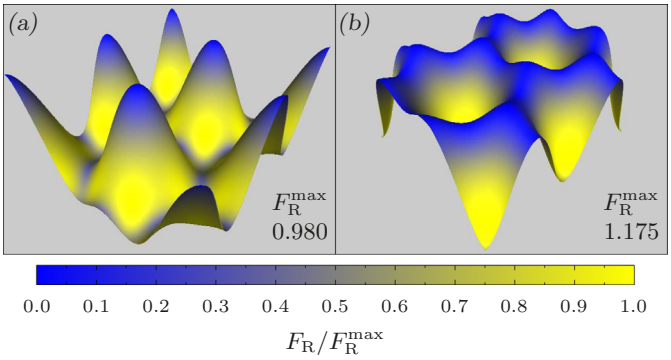

Fig. 4. Redeposition F_{R} on hexagonally arranged dot (a) and hole (b) structures with an aspect ratio of $\epsilon = 1$, $V_{\text{a}}J = 1$, $Y = Y_{\text{const}}$ and $f = f_{\text{skew}}$.

a sticking coefficient of unity, the actual ratio of redeposition might be lower, but these results clearly point out that the effect of redeposition has to be considered for the mentioned experimental surfaces.

3.2 Redeposition distribution on the surface

Although the redeposition ratio has already shown fundamental features of the redeposition mechanism, it does not provide any information about the spatial distribution of the redepositing particles. In Figure 4 two surfaces and the corresponding color-coded redeposition F_{R} are depicted. It can be clearly seen that the slopes near the valleys are subject to maximum redeposition, whereas no particles reattach at the topmost surface regions. This is a general property of redeposition since it can be qualitatively found independently of the aspect ratio and the specific model for Y and f. Furthermore, it is apparent from Figure 4 that $F_{\text{R}}(\mathbf{x}_{\text{R}})$ can be approximately considered as a function of the surface height H_{R} instead of $\mathbf{x}_{\text{R}}$, although the function $H(\mathbf{x})$ defined by (29) cannot be inverted to obtain $\mathbf{x}_{\text{R}}$ from H_{R}. The validity of the approximative functional relationship $F_{\text{R}}(H)$ will be further discussed in the following sections.

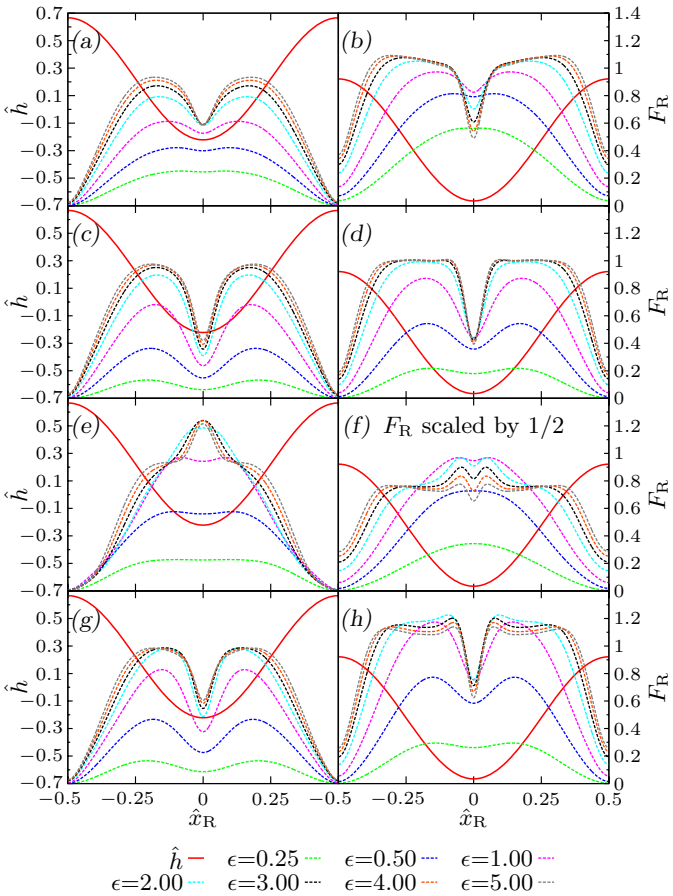

Fig. 5. Cross-sectional plots of the normalized surface height $\hat{h}$ and the corresponding redeposition F_{R}. Left column: dot structures. Right column: hole structures. We have set $V_{\text{a}}J = 1$ and $Y = Y_{\text{const}}$. The angular erosion distributions are (a,b) f_{const}, (c,d) $f_{\cos\theta}$, (e,f) f_{spec}, (g,h) f_{skew}. In (f) $F_{\text{R}}/2$ is depicted for the sake of visibility.

Due to this relation, it is possible to depict the qualitative redeposition profile by plotting cross-sections of the surface and the corresponding redeposition F_{R} instead of color-coded three-dimensional plots like in Figure 4. These cross-sectional data is shown in Figure 5 for both investigated hexagonally arranged morphologies, different aspect ratios ϵ and the considered models for f. The cross-section for dot structures ranges from one hilltop to an adjacent one, whereas the same orientation was used for holes. It is clearly visible that, independently whether dots or holes are considered, minimum redeposition appears on the topmost surface areas. Since the chosen cross-section does not intersect the maximum of H for the holes, a non-vanishing redeposition F_{R} can be found at $x_{\text{R}} = \pm 1/2$ in the right column of Figure 5. The particles redepositing there stem from erosion positions around the global maxima of the surface beside the cross-section area. Most of the redeposition curves in Figure 5 show a bimodal profile with a local minimum at the valley surrounded by global redeposition maxima at the valley-near slopes. Only the case f_{spec} exhibits a more complicated behavior which is a result of the strongly preferred erosion into the grazing

direction towards the valleys. However, in particular for physically realistic aspect ratios $\epsilon \lesssim 1$, the explicit angular erosion distribution has no considerable qualitative impact on the redeposition effect. This fact can also be observed in the one-dimensional continuum model [52] and in the one-dimensional discrete solid-on-solid redeposition model [49].

3.3 Approximation of F_R

Due to its complexity, one is interested in approximations for the redeposition model (11). However, the presence of the visibility function v_H impedes analytical expansions of F_R. Thus, simple approximations for F_R can only be obtained by analyzing the numerical data of F_R by means of curve fitting or similar methods.

Particularly with regard to the damping term, we are interested in an approximation of F_R in terms of the normalized relative surface height $\hat{h}$. However, besides height differences, there are also gradient terms that enter the redeposition model F_R (cf. Eqs. (3), (7)–(9)). When curvature-dependent sputtering is neglected, higher spatial derivatives do not occur in the redeposition model. Therefore, we include a local gradient term into our approximation. Since ∇H already fulfills the scale-invariance, the gradient dependence need not be written in terms of the normalized quantities. A minimal approximation $F_R^{\text{app.}} \approx F_R$ that is able to fit the numerical data very well is the following:

$$F_R^{\text{app.}} = F_{R,0} + \hat{b}\hat{h} + \hat{c}\hat{h}^2 + \left(d + \hat{p}\hat{h} + \hat{q}\hat{h}^2\right) \cdot (\nabla H)^2 \,. \quad (33)$$

Each of the coefficients $F_{R,0}$, $\hat{b}$, $\hat{c}$, d, $\hat{p}$ and $\hat{q}$ are functions of the aspect ratio ϵ and depend on the choice of f, Y and the specific morphology. Besides a term of zeroth order $F_{R,0}$ and a linear damping term, a quadratic damping term is considered. The gradient term of lowest order is weighted with the same functional form as the non-gradient portion of the approximation. The specific approximation ansatz (33) will be substantiated in this section and later on in Section 4.2.

The approximation $F_R^{\text{app.}}$ can be written in terms of the non-normalized height H, i.e.

$$\begin{aligned} F_R^{\text{app.}} = {} & F_{R,0} + b\left(H - \bar{H}\right) + c\left(H - \bar{H}\right)^2 \\ & + \left(d + p\left(H - \bar{H}\right) + q\left(H - \bar{H}\right)^2\right) \cdot (\nabla H)^2 \,, \end{aligned} \quad (34)$$

using the relations $b = \hat{b}/A$, $c = \hat{c}/A^2$, $p = \hat{p}/A$ and $q = \hat{q}/A^2$.

In order to obtain the coefficients of (33), we have numerically calculated F_R. By arranging the corresponding triple $(\hat{h}, (\nabla H)^2, F_R)$ in a three-dimensional coordinate system, the resulting points can be fitted by the approximation (33) via the six fit coefficients. A representative plot of this procedure is depicted in Figure 6. The approximation $F_R^{\text{app.}}$ resembles the numerical data very well and,

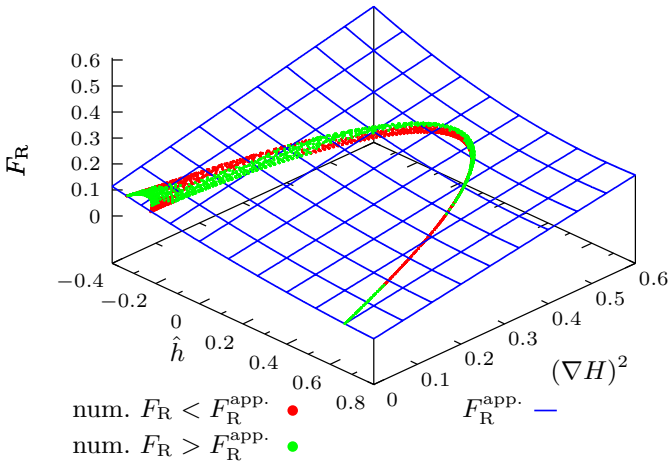

Fig. 6. Numerically determined redeposition F_R plotted versus relative height $\hat{h}$ and squared slope $(\nabla H)^2$ (here for hexagonal dots, $\epsilon = 0.25$, f_{skew}, Y_{const}). A least square fit determines the coefficients of the approximation $F_R^{\text{app.}}$. For the sake of visibility, the numerical data for F_R below and above $F_R^{\text{app.}}$ is indicated by red and green points, respectively.

due to the inclusion of the gradient portion, the coarsening of the point data in the valleys is resolved. When the gradient part in (33) is not considered, the resulting approximation just in terms of the relative surface height shows strong deviations from the numerical data. Furthermore, the approximation only with $F_{R,0}$-, $\hat{b}$- and $\hat{c}$-term is not able to reproduce the dynamical influence of redeposition in spatio-temporal surface evolution, which will be discussed later on in Section 4.2.

The approximated coefficients of $F_R^{\text{app.}}$ as function of the aspect ratio ϵ are depicted in Figure 7 for representative models for Y and f and for dots and holes. Independently of the morphology and the models for the sputter yield and angular erosion distribution, a negative damping coefficient $\hat{b}$ can be found. Thus, redeposition has a contribution with the functional form of a linear damping term, but with a coefficient depending on the aspect ratio. $\hat{b}$ sets in with ϵ for the case f_{const} and with ϵ^2 in all other cases. This result was expected with respect to the discussion in Section 2.2.4. Similarly, a quadratic damping term can be observed. The corresponding coefficient $\hat{c}$ is positive for the dot structures and also for hole structures with a small aspect ratio. For hole morphologies with higher aspect ratios, however, $\hat{c}$ is negative.

While the coefficient $F_{R,0}$ does not influence the pattern formation process, a fundamental contribution is given by the term $d(\nabla H)^2$. Since the latter is a scale invariant quadratic term, it is already present for $\epsilon \to 0$ and it diverges in this limit for the isotropic erosion distribution f_{const} due to the linear onset of redeposition with the aspect ratio. However, independently of the specific models and the morphology, a positive coefficient d can be found. This reflects the fact that tilted regions on patterned surfaces face towards adjacent structures, which leads to an increased solid angle $d\Omega$ and, thereby, to an enhanced redeposition effect on these areas. The positive

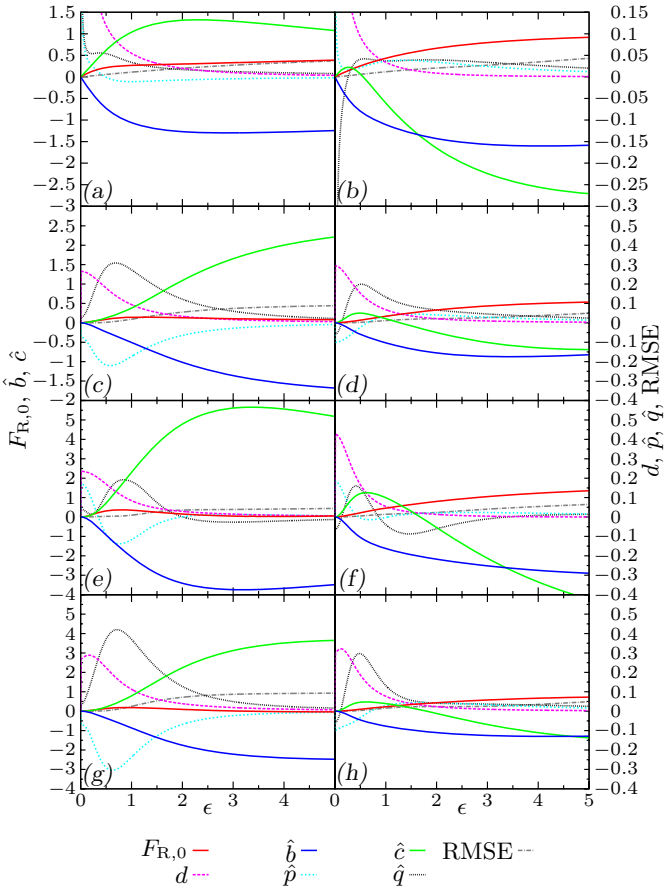

Fig. 7. Fitted coefficient of (33) as function of ϵ for the different models for f and for hexagonally arranged dots (left column) and holes (right column) with $Y = Y_{\mathrm{const}}$. (a,b): f_{const}, (c,d): $f_{\cos\theta}$, (e,f): f_{spec}, (g,h): f_{skew}.

contribution to the nonlinear term $(\nabla H)^2$ extends the interpretation of this term in the KS erosion model. We will discuss this fact later on in Section 4.2.

Besides the discussed coefficients, there are also corrections of higher order, corresponding to the $\hat{p}$- and $\hat{q}$-coefficients, present in the approximation. These start at $\epsilon \to 0$ with a non-vanishing value (divergence in case of f_{const}), whereas the corresponding coefficients tend to zero in the limit of high aspect ratios. Additionally, the rms error

$$\mathrm{RMSE} = \left(\frac{1}{\sqrt{3}L^2} \int_0^{\sqrt{3}L} dx_{\mathrm{R}} \int_0^{L} dy_{\mathrm{R}} \times \left[F_{\mathrm{R}}(\mathbf{x}_{\mathrm{R}}) - F_{\mathrm{R}}^{\mathrm{app.}}\left(\hat{h}(\mathbf{x}_{\mathrm{R}}), (\nabla H_{\mathrm{R}})^2 \right) \right]^2 \right)^{1/2} \tag{35}$$

is depicted. Even in the limit of extreme aspect ratios the deviation RMSE is below 0.1 for all investigated morphologies and angular erosion distributions.

Since the approximation (20) is valid for $f_{\cos\theta}$ and f_{skew}, the quadratic onsets of the coefficient curves in Figure 7 coincide with the small-gradient approximation $F_{\mathrm{R}}^{\mathrm{B}}$

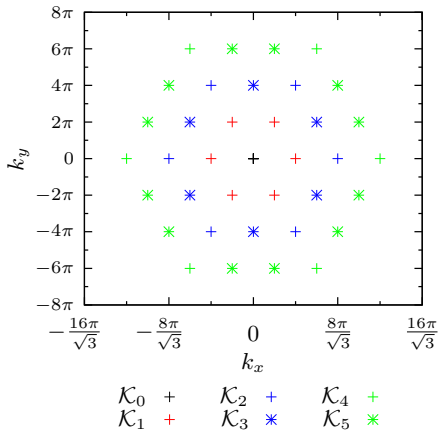

Fig. 8. Considered spatial Fourier modes in the decomposition of F_{R}. Besides the DC mode (black) and the basic mode (red), we have taken quadratic (blue) and cubic (green) couplings into account.

for $\epsilon \approx 0$ in these cases. The numerical values of the corresponding coefficients for $F_{\mathrm{R}}^{\mathrm{B}}$ are listed in Appendix B.

3.4 Fourier analysis

The coefficients of the approximation $F_{\mathrm{R}}^{\mathrm{app.}}$ were determined by the method of least squares, i.e. by minimizing RMSE. Another way to get insight into the redeposition mechanism is the Fourier analysis, focusing on the lower order harmonics only. Instead of minimizing the residual RMSE via fit coefficients, the Fourier decomposition gives exact results for the effect of redeposition on the subspace spanned by the considered modes, whereas higher harmonics are not taken into account. We investigate F_{R} by the following Fourier ansatz up to the third harmonics:

$$F_{\mathrm{R}}(\hat{\mathbf{x}}_{\mathrm{R}}) \approx F_{\mathrm{R}}^{\mathrm{FT}}(\hat{\mathbf{x}}_{\mathrm{R}}) = \tilde{F}_0 + \sum_{i=1}^{5} \tilde{F}_i(\epsilon) g_i(\hat{\mathbf{x}}_{\mathrm{R}})$$
$$\text{with} \quad g_i(\hat{\mathbf{x}}_{\mathrm{R}}) = \frac{1}{2} \sum_{\mathbf{k} \in \mathcal{K}_i} \exp\left(i\mathbf{k}\cdot\hat{\mathbf{x}}_{\mathrm{R}}\right). \tag{36}$$

The corresponding wave vectors $\mathbf{k}$ are depicted in Figure 8. The sets $\mathcal{K}_i = \{\mathbf{k}_{i,1}, \ldots, \mathbf{k}_{i,N_i}\}$ (with $i = 0, \ldots, 5$) each comprise the modes that have the same amplitude $\tilde{F}_i$ due to the symmetry of the surface. The numbers N_i of amplitudes are $N_0 = 1$ and $N_5 = 12$, whereas $N_i = 6$ holds for the other cases $i = 1, 2, 3, 4$.

Using the orthogonality of the Fourier decomposition, we are able to extract the amplitudes $\tilde{F}_i$ and, thereby, the effect of redeposition on the harmonics of the surface pattern. In Figure 9 the extracted Fourier amplitudes are depicted as function of the aspect ratio ϵ and for the different morphologies and models for f. The DC offset $\tilde{F}_0$ was omitted, but since the relation $\tilde{F}_0 = \eta$ holds for the choice Y_{const}, $\tilde{F}_0$ can be read off from Figure 3. From the coefficient $\tilde{F}_1$ in Figure 9 it can be seen that redeposition has a damping effect on the surface base modes. This is

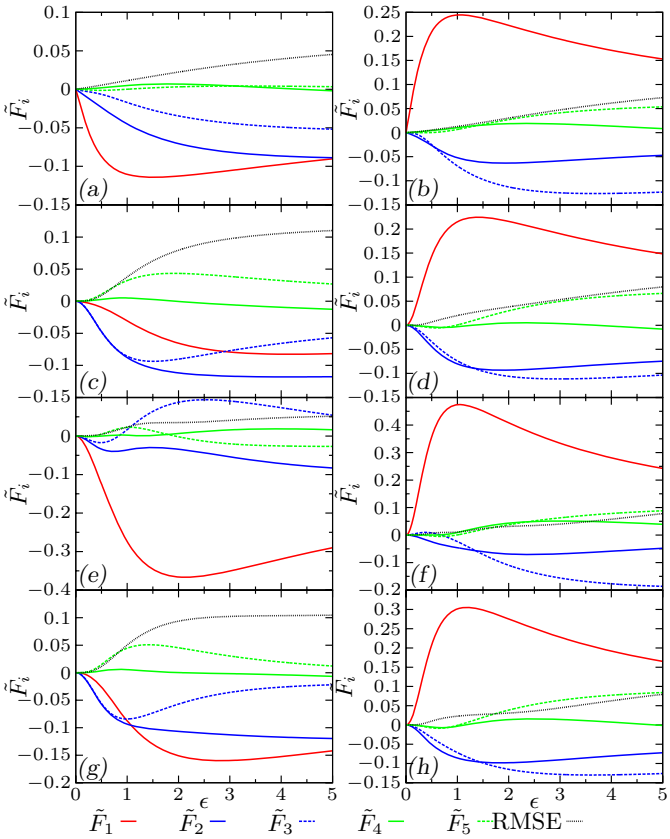

Fig. 9. Amplitudes of the Fourier decomposition (36) for dots (left column) and holes (right column) with $Y = Y_{\text{const}}$. (a,b) f_{const}, (c,d) $f_{\cos\theta}$, (e,f) f_{spec}, (g,h) f_{skew}.

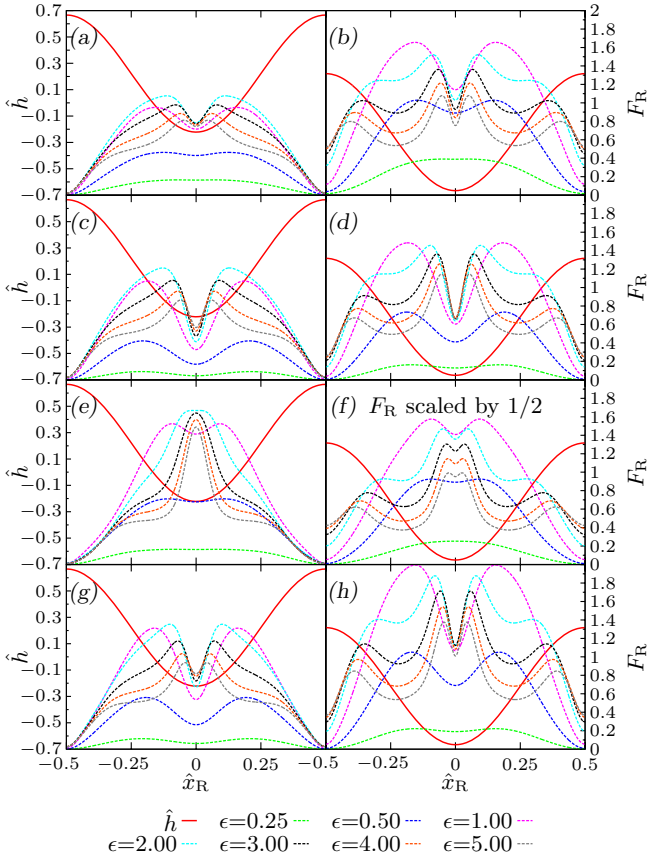

Fig. 10. Same as Figure 5, but for the tilt-dependent sputter yield Y_{tilt}.

because $\hat{h}(\hat{\mathbf{x}}_{\text{R}}) = \pm(2/9)g_1(\hat{\mathbf{x}}_{\text{R}})$ holds for dots (+) and holes (−) and $\tilde{F}_1$ has the opposite sign in each case.

The coefficients $\tilde{F}_2$ and $\tilde{F}_3$ belonging to the quadratic couplings are – with the exception of f_{spec} – always negative. While the cubic couplings $\tilde{F}_4$ and $\tilde{F}_5$ are typically only present at higher aspect ratios, $\tilde{F}_5$ is pronounced with positive values for the models $f_{\cos\theta}$ or f_{skew} on dot morphologies. Furthermore, these configurations exhibit a much higher deviation RMSE (defined analogously to Eq. (35) with $F_{\text{R}}^{\text{app.}}$ substituted by F_{R}^{FT}) than the other ones. This means that there are nonlinearities of fourth or higher order present in F_{R} which are not considered by the ansatz (36).

We have also investigated the small-gradient approximation F_{R}^{B} (cf. Eq. (20)) by means of Fourier decomposition. The corresponding coefficients, which also resemble the quadratic increases for $f_{\cos\theta}$ or f_{skew} at $\epsilon \approx 0$, can be found in Appendix B.

3.5 Influence of the sputter yield

For simplicity we have chosen the model Y_{const} up to here. A more physical realistic investigation of the redeposition mechanism has to consider two characteristics of the sputter yield, namely the tilt- and the curvature-dependence of Y.

3.5.1 Tilt-dependent sputter yield

For the tilt-dependence we use the model Y_{tilt} (cf. Eq. (22)). Analogously to Figure 5, cross-sections of the surface and the corresponding redeposition F_{R} are depicted in Figure 10. As expected from the small-gradient expansion (18), the tilt-dependence of Y has no impact for small aspect ratios. Since $Y_0 < 1 = Y_{\text{const}}$ was chosen, the curves in Figure 10 for $\epsilon = 0.25$ are below the corresponding ones in Figure 5, but the qualitative shape is exactly the same. With increasing ϵ, however, the tilt-dependence of the sputter yield has a visible effect on F_{R}: on the one hand, the enhanced erosion at the slopes leads to an increase of the overall redeposition and, on the other hand, the shape of the cross-sectional curves is altered for extreme high aspect ratios. In particular, there are additional local maxima of F_{R} at slopes near the hilltops of the hexagonal hole morphologies, which can be understood as follows: as we will see later on in Section 3.6, the redepositing particles for high aspect ratios stem from erosion events taking place at approximately the same height, i.e. $\hat{h}_{\text{R}} \approx \hat{h}_{\text{E}}$. Since Y_{tilt} has its maximum at slopes with an angle of $\alpha_{\max}$, these surface regions are subject to maximum redeposition with particles stemming from erosion at the opposing slopes.

For extremely high aspect ratios the entire redeposition profiles are diminished due to the decrease of Y_{tilt} for $\alpha \to \pi/2$.

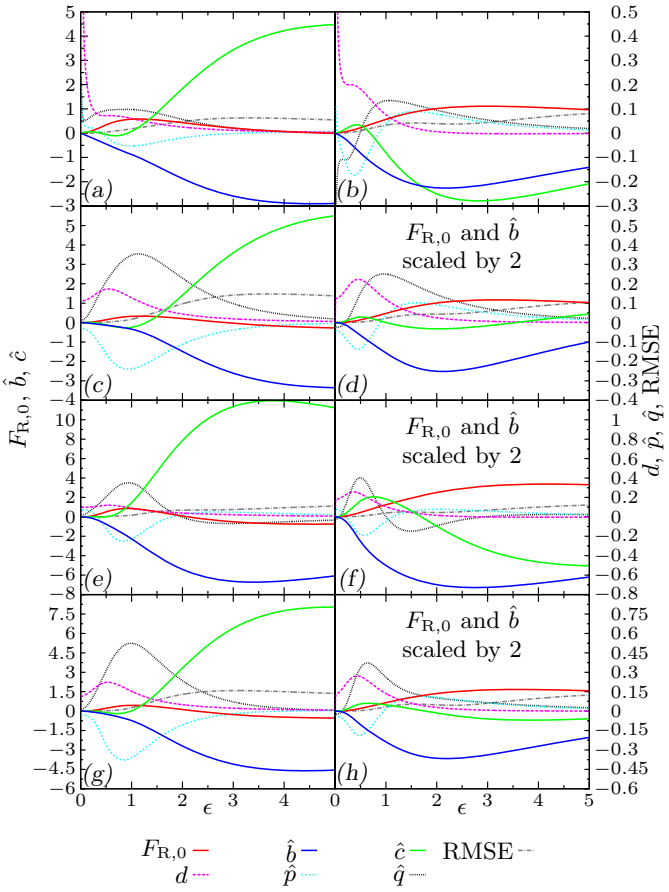

Fig. 11. Same as Figure 7, but for the tilt-dependent sputter yield Y_{tilt}.

The graphs of the corresponding fit coefficients in Figure 11 show in comparison with those with Y_{const} in Figure 7 the following main differences: Again, $\hat{b} < 0$ holds for all configurations, but $\hat{c}$ can now become negative for small ϵ on hill structures. The curves of the coefficient d now show a maximum at around $\epsilon \approx 0.5$ which can be attributed to the increase of $Y_{\text{tilt}}(\alpha)$ for moderate α.

In particular for physically reasonable aspect ratios, however, the tilt-dependence of the sputter yield has only a quantitative impact on the redeposition mechanism.

3.5.2 Curvature-dependence of Y

Due to the Bradley-Harper effect, the sputter yield Y also depends on the local surface curvature K, which can be approximated by the Laplacian $K = \nabla^2 H$. This dependency breaks the scale invariance (14) for the sputter yield and, thereby, also for the redeposition F_{R}. However, to the lowest order, the Bradley-Harper mechanism can be written by decomposing

$$Y(\alpha, K) = Y(\alpha) + \Gamma(\phi) \cdot K. \tag{37}$$

Here, the first term on the rhs comprises the pure incident angle portion of Y, whereas the second addend models the Bradley-Harper mechanism. Strictly speaking, Γ is a function of the incidence angle α as well, but it is typically evaluated at the global incidence angle ϕ [22,25], which is $\phi = 0°$ for normal incidence. We have set $\Gamma = 1$ in the following. With the decomposition (37), the redeposition can be expressed in the same manner:

$$F_{\text{R}} = \text{equation (11)} \; + \; \Gamma(\phi) \cdot F_{\text{R}}^{K} \tag{38}$$

with the curvature portion of the redeposition mechanism

$$F_{\text{R}}^{K} = JV_{\text{a}} \int d^2 x_{\text{E}} \, v_H(\mathbf{x}_{\text{R}}, \mathbf{x}_{\text{E}}) \left(\nabla^2 H_{\text{E}}\right) f(\alpha, \theta, \varphi) \times \frac{\Delta \mathbf{x} \cdot \nabla H_{\text{R}} - \Delta H}{\left[(\Delta x)^2 + (\Delta H)^2\right]^{3/2}}. \tag{39}$$

The latter resembles the functional form of (11) with $Y(\alpha)$ exchanged by $(\nabla^2 H_{\text{E}})$. Contrarily to the entire redeposition F_{R}, the curvature-dependent portion F_{R}^{K} can also be negative. Furthermore, when keeping the aspect ratio $\epsilon = A/L$ constant, F_{R}^{K} is inversely proportional to both A and L, respectively.

In order to provide results that are independent of the amplitude A and the characteristic length L, $F_{\text{R}}^{K}(\hat{x}_{\text{R}}) \cdot A$ or $F_{\text{R}}^{K}(\hat{x}_{\text{R}}) \cdot L$ are good quantities to be plotted. In Figure 12, $F_{\text{R}}^{K}(\hat{x}_{\text{R}}) \cdot L/\epsilon$ is depicted, where the division by ϵ was performed for the sake of visibility. The curvature-dependence of the sputter yield enhances the redeposition in the valley regions, whereas the hilltops are subject to a reduced amount of redepositing particles. With increasing aspect ratio, F_{R}^{K} takes on values that exceed the ones of the curvature-independent portion by far. However, from the physical point of view, the total sputter yield (37) may not become negative anywhere on the surface. Thus, for surfaces with higher curvatures, the choice of the coefficient $\Gamma = 1$ can be too large.

We can perform an analogous fit procedure for F_{R}^{K} by choosing the approximation

$$F_{\text{R}}^{K} \approx F_{\text{R}}^{K,\text{app.}} = F_{\text{R},0}^{K} + \hat{b}^{K} \hat{h} + \hat{c}^{K} \hat{h}^2 + \left(d^{K} + \hat{p}^{K} \hat{h} + \hat{q}^{K} \hat{h}^2\right) \cdot (\nabla H)^2 . \tag{40}$$

The resulting coefficient graphs are plotted in Figure 13. Since $\hat{b}^{K} < 0$ holds, the Bradley-Harper effect enhances the damping effect of the redeposition mechanism on the surface basic mode, whereas $\hat{c}^{K}$ is positive for all configurations. The results are similar to our one-dimensional investigation of the redeposition mechanism [52].

3.6 Erosive origin of redepositing particles

Hitherto, we have extracted a lot of information regarding the redeposition distribution on the surface. However, we have not investigated the origin of the redepositing particles yet, i.e. their position of erosion $\mathbf{x}_{\text{E}}$, where they have left the surface before reattaching to it again at $\mathbf{x}_{\text{R}}$. In order to provide presentable information about the erosion distribution, we express the vectorial coordinates $\mathbf{x}_{\text{R}}$

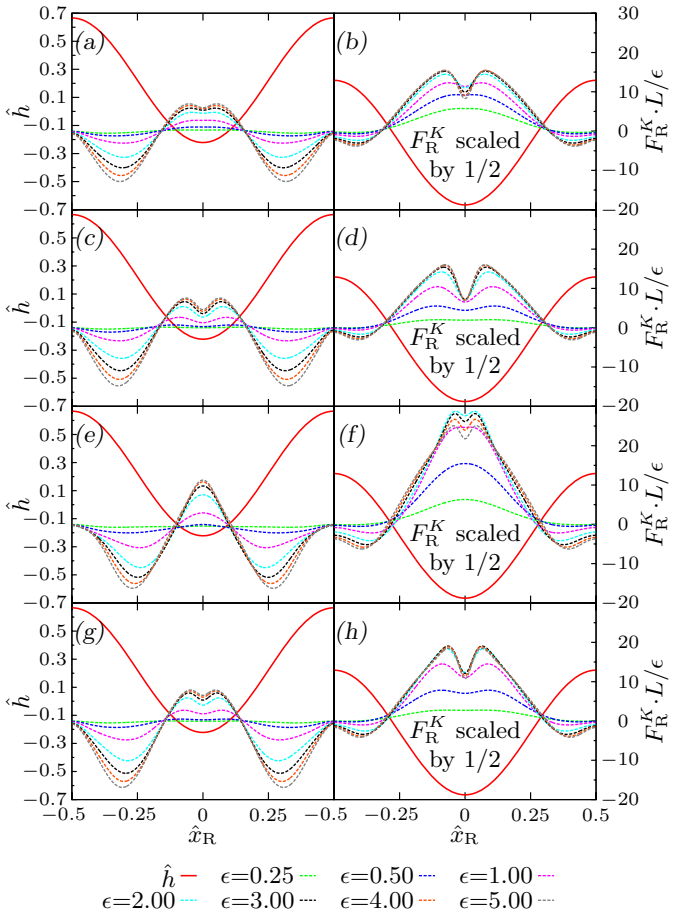

Fig. 12. Cross-sectional plots of the curvature-dependent portion F_R^K for dots (left column) and holes (right column). (a,b) f_{const}, (c,d) $f_{\cos\theta}$, (e,f) f_{spec}, (g,h) f_{skew}.

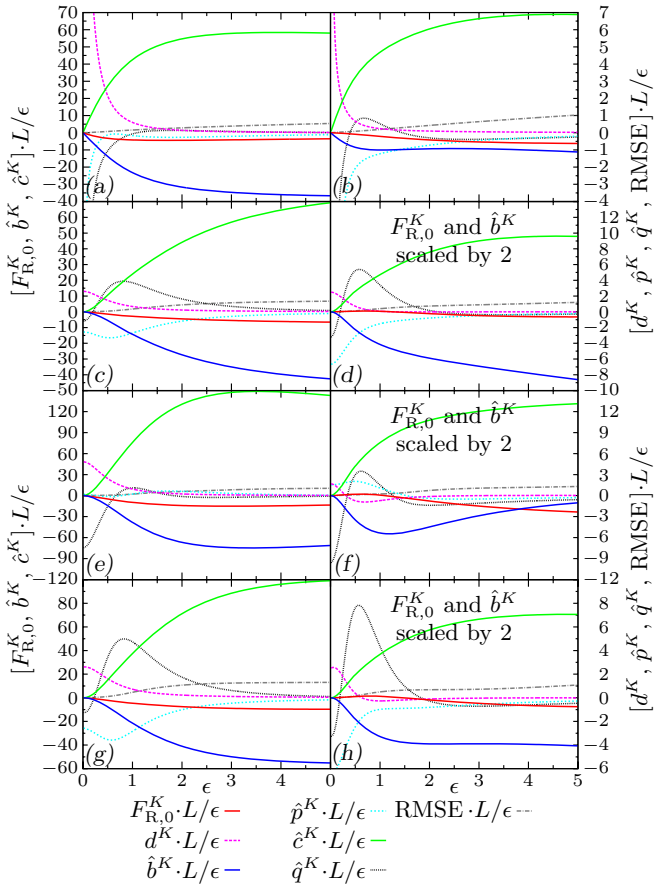

Fig. 13. Corresponding fit coefficients for F_R^K. Parameters as in Figure 12.

and $\mathbf{x}_E$ by averaged scalar quantities. The positions of redeposition $\mathbf{x}_R$ are once more expressed by the normalized height $\hat{h}_R$ and, instead of $\mathbf{x}_E$, we are more interested in the distribution with respect to the normalized lateral distance

$$\hat{D}_{ER} = \frac{\|\mathbf{x}_E - \mathbf{x}_R\|}{L} = \|\hat{\mathbf{x}}_E - \hat{\mathbf{x}}_R\| \tag{41}$$

between the erosion event and the redeposition event. We can obtain the distribution $\rho_{\hat{D}}(\hat{h}_R, \hat{D}_{ER}) d\hat{h}_R d\hat{D}_{ER}$ of particles that redeposit on a height interval between $\hat{h}_R$ and $\hat{h}_R + d\hat{h}_R$ after being eroded in a normalized distance between $\hat{D}_{ER}$ and $\hat{D}_{ER} + d\hat{D}_{ER}$ by the relation:

$$\begin{aligned}\rho_{\hat{D}}\left(\hat{h}_R, \hat{D}_{ER}\right) = \frac{JV_a}{N_{\hat{h}}(\hat{h}_R)} \int d^2x_R \int d^2x_E \, v_H(\mathbf{x}_R, \mathbf{x}_E) \\ \times Y(\alpha) f(\alpha, \theta, \varphi) \frac{\Delta\mathbf{x} \cdot \nabla H_R - \Delta H}{[(\Delta\mathbf{x})^2 + (\Delta H)^2]^{3/2}} \\ \times \delta\left(\frac{H(\mathbf{x}_R)}{A} - \hat{h}_R\right) \\ \times \delta\left(\frac{\|\mathbf{x}_E - \mathbf{x}_R\|}{L} - \hat{D}_{ER}\right).\end{aligned} \tag{42}$$

Here, $\hat{h}_R$ and $\hat{D}_{ER}$ have to be considered now as independent variables and δ is the Dirac delta function. We have normalized the distribution $\rho_{\hat{D}}$ by the factor

$$N_{\hat{h}}\left(\hat{h}_R\right) = \int d^2x_R \, \delta\left(\frac{H(\mathbf{x}_R)}{A} - \hat{h}_R\right) \tag{43}$$

to cancel out the length of the level curve at the considered height $\hat{h}_R$.

The erosion distance distribution $\rho_{\hat{D}}$ is depicted in Figure 14 with the parameters Y_{tilt} and f_{skew}. The maximum of $\rho_{\hat{D}}$ is always located within the range $\hat{D}_{ER} < 1$. Thus, most of the redepositing particles were eroded within the real distance of a characteristic lateral length L. While in the valleys (negative $\hat{h}_R$) the maximum contribution stems from the erosion at positions in close vicinity ($\hat{D}_{ER} \approx 0$) of the redeposition event, it is apparent that on hilltops (positive $\hat{h}_R$) the redepositing particles were eroded on the facing areas of the adjacent structures ($0.25 \lesssim \hat{D}_{ER} < 1$). A fundamental difference between the hexagonally arranged dot patterns (left column) and the corresponding hole patterns (right column) is the contribution of particles eroded at distant regions of the surface. On the dot morphology, erosion at structures in a distance of up to four dot-to-dot-distances L can have an effect on the redeposition. In contrast, the maximum range between erosion

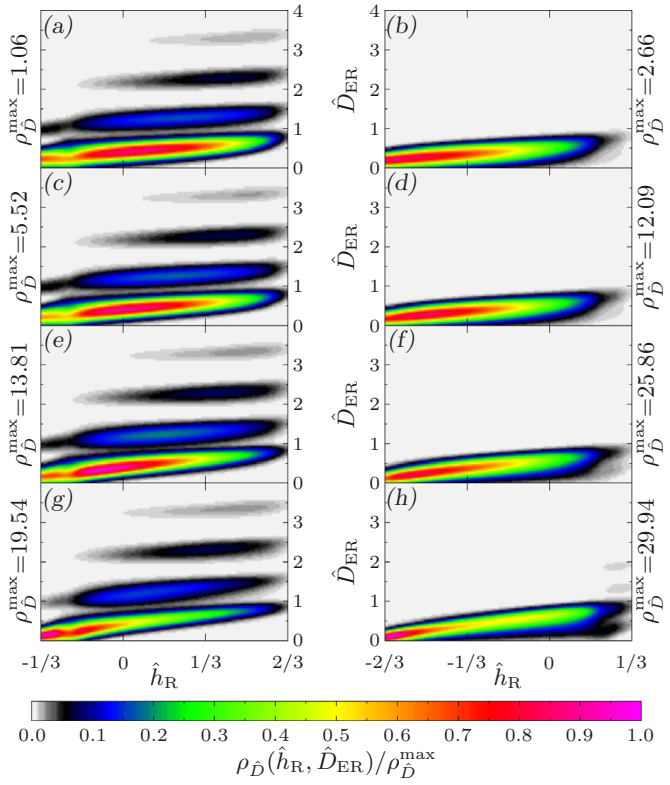

Fig. 14. Distance distribution $\rho_{\hat{D}}$ between the positions of erosion and redeposition for Y_{tilt}, f_{skew} on a dot (left column) and hole pattern (right column), respectively. The aspect ratio ϵ is (a,b) 0.25, (c,d) 0.5, (e,f) 1.0, (g,h) 2.0.

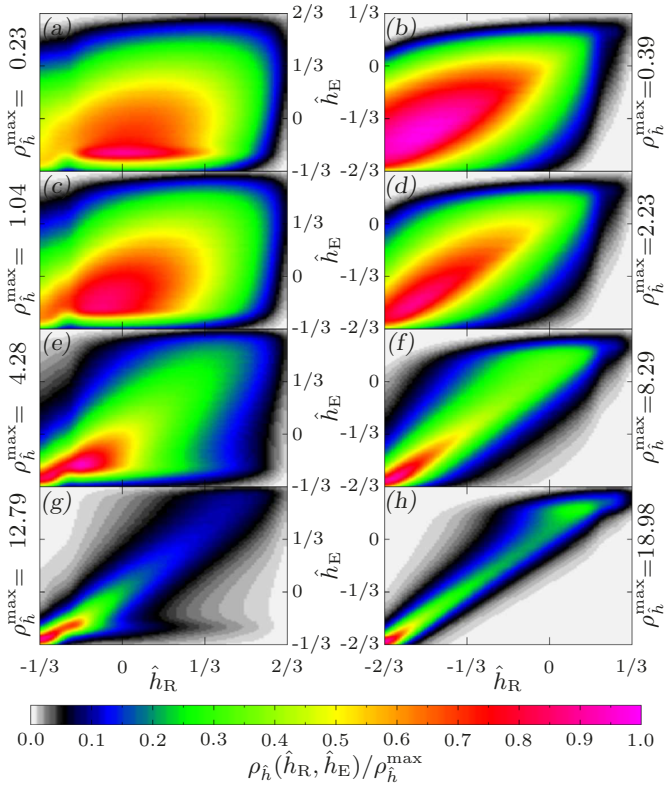

Fig. 15. Erosion and redeposition height distribution $\rho_{\hat{h}}$ between the positions of erosion and redeposition for Y_{tilt}, f_{skew} on a dot (left column) and hole pattern (right column), respectively. The aspect ratio ϵ is (a,b) 0.25, (c,d) 0.5, (e,f) 1.0, (g,h) 2.0.

and redeposition is almost entirely trapped within each single well of the hole structures. An increase of the aspect ratio does not alter the characteristics of $\rho_{\hat{D}}$, except that the global maximum of $\rho_{\hat{D}}$ is shifted more to erosion and redeposition in the same valley, i.e. minimal $\hat{h}_{\mathrm{R}}$ and $\hat{D}_{\mathrm{ER}} \approx 0$.

We can also investigate the distribution in terms of the erosion height $\hat{h}_{\mathrm{E}}$ by defining analogously to equation (42) the distribution

$$\begin{aligned}\rho_{\hat{h}}\left(\hat{h}_{\mathrm{R}}, \hat{h}_{\mathrm{E}}\right) = \frac{JV_{\mathrm{a}}}{N_{\hat{h}}(\hat{h}_{\mathrm{R}})} \int d^2x_{\mathrm{R}} \int d^2x_{\mathrm{E}}\, v_H(\mathbf{x}_{\mathrm{R}}, \mathbf{x}_{\mathrm{E}}) \\ \times Y(\alpha) f(\alpha, \theta, \varphi) \frac{\Delta\mathbf{x}\cdot\nabla H_{\mathrm{R}} - \Delta H}{\left[(\Delta\mathbf{x})^2 + (\Delta H)^2\right]^{3/2}} \\ \times \delta\left(\frac{H(\mathbf{x}_{\mathrm{R}})}{A} - \hat{h}_{\mathrm{R}}\right) \cdot \delta\left(\frac{H(\mathbf{x}_{\mathrm{E}})}{A} - \hat{h}_{\mathrm{E}}\right). \end{aligned} \tag{44}$$

In Figure 15, it can be read off from the plotted data for $\rho_{\hat{h}}$ that for small aspect ratios the redeposition at almost every height $\hat{h}_{\mathrm{R}}$ is constituted by erosion events happening at almost the whole range of erosion heights $\hat{h}_{\mathrm{E}}$. Only particles eroded in the close vicinity of the surface height maxima ($\hat{h}_{\mathrm{E}} = \max$) do not contribute to the redeposition. Similarly, particles eroded at the lowest regions of the surface ($\hat{h}_{\mathrm{E}} = \min$) cannot reach the highest parts of the surface for redeposition ($\hat{h}_{\mathrm{R}} = \max$). With increasing aspect ratio, the distribution $\rho_{\hat{h}}$ focuses around the line $\hat{h}_{\mathrm{E}} = \hat{h}_{\mathrm{R}}$. This behavior can be understood by taking the limit of high aspect ratios: if $\hat{h}_{\mathrm{E}}$ differs from $\hat{h}_{\mathrm{R}}$, the influence of the non-normalized height difference ΔH becomes large within the distance vector $\mathbf{\Delta}$. This leads a vanishing solid angle $d\Omega$ (cf. Eq. (9)) and thereby to a small redeposition contribution. Furthermore, it can be seen that the global maximum of $\rho_{\hat{h}}$ moves to the valleys for high aspect ratios, just as we have noticed it in the previous discussion of the distribution $\rho_{\hat{D}}$.

4 Spatio-temporal evolution with redeposition

In our letter [53], we have already briefly reported the pattern-stabilizing effect that redeposition can have in combination with erosion. Here, we will present a thorough investigation of this effect by discussing different parameter combinations, a stability map as well as the interplay with other erosion models besides the Kuramoto-Sivashinsky equation.

With the redeposition model (11) substituted in the general height evolution (2), we only have to specify the erosion model F_{E}. Since it is the minimal model, i.e. the one with the lowest number of parameters, we use

the Kuramoto-Sivashinsky equation

$$F_{\mathrm{E}} = a_0 + a_1\nabla^2 H + a_2\nabla^4 H + a_3\left(\nabla H\right)^2 \qquad (45)$$

as erosion model for the moment. By combining F_{E} with F_{R}, transforming into the coordinate system co-moving with a_0 and rescaling the resulting equation by:

$$x \to \sqrt{\frac{a_2}{a_1}}\,x, \quad H \to \sqrt{\frac{a_2}{a_1}}\,H, \quad t \to -\frac{a_2}{a_1^2}\,t,$$
$$\beta = V_{\mathrm{a}}J\sqrt{\frac{a_2}{a_1^3}} \quad \text{and} \quad \kappa = a_3\sqrt{\frac{a_2}{a_1^3}}, \qquad (46)$$

the model reads

$$\partial_t H = \beta F_{\mathrm{R}} - \nabla^2 H - \nabla^4 H + \kappa\left(\nabla H\right)^2. \qquad (47)$$

Here, we have neglected the influence of the Bradley-Harper effect within F_{R} to take advantage of the scale-invariance. Additionally, we have assumed $a_1 < 0$, corresponding to a roughening instability of the flat surface, and $a_2 < 0$, i.e. a Mullins diffusion that counteracts the instability at large wave numbers. Since the factor $V_{\mathrm{a}}J$ has now be included to the parameter β, it has to be set to unity within F_{R} in the combined evolution equation (47).

4.1 Influence of redeposition on the pattern formation

We start our analysis of the combined model equation (47) by discussing representative simulation results for specific parameters. Since the models Y_{tilt} and f_{skew} are the most physical ones, we will primarily focus on these. However, we will also address some other model combinations later on. The left column of Figure 16 shows the evolution of an initially almost flat surface subject to the combined erosion and redeposition according to the model equation (47) with[2] $\beta = 2.0$ and $\kappa = -0.4$. At early times of the evolution, the linear portion $-(\nabla^2 + \nabla^4)H$ in the model equation leads to a growth of lateral Fourier modes with wave numbers k between $0 < k < 1$. Then, with increasing roughening, redeposition and the κ-nonlinearity set in, the roughening saturates and a more and more ordered hexagonally arranged dot pattern organizes on the surface. The remaining defects dissolve for longer simulation times and the surface converges to a perfect hexagonal arrangement. Besides the qualitative similarity of the resulting pattern in comparison with experimentally observed dot morphologies, we can also notice a quantitative agreement: the aspect ratio has a value of $\epsilon = 0.76$ ($A = 6.62$ and $L = 8.74$) and is therefore comparable to the dot morphologies found on binary compounds [6–11] and by irradiation with heavy Bi-(cluster)-ions [12–17]. Since we had to use the same scales for $\hat{h}$ and $\mathbf{x}$ in (46), the aspect ratio is a characteristic quantity of the model

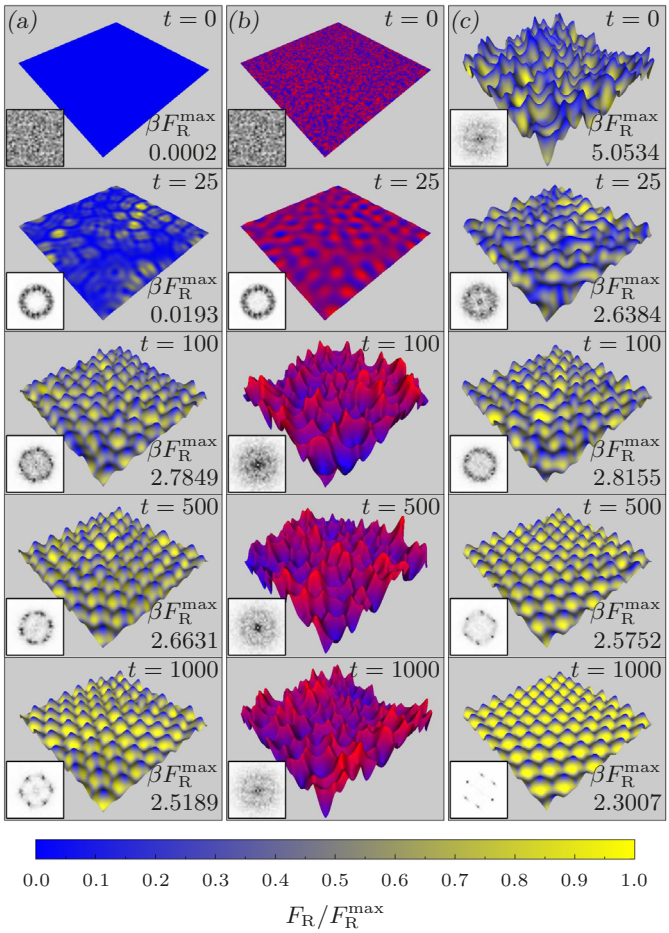

Fig. 16. (a) Evolution of the combined model equation (47) with Y_{tilt}, f_{skew}, $\beta = 2.0$ and $\kappa = -0.4$. (b) Same parameters, but without redeposition, i.e. $\beta = 0$. (c) With redeposition, same parameters as in (a), but starting from a chaotic initial surface. The insets show the corresponding PSDs.

equation (47), which cannot be adjusted by rescaling the height or the lateral extent. The redeposition F_{R} shows again the typical distribution on the surface, i.e. no redeposition on hills and maximum redeposition on the slopes near the valley.

The well-ordered structures are triggered by redeposition within the model equation (47). This is strikingly apparent by the comparison with the evolution shown in Figure 16b. Here, a simulation run based on the same initial surface and parameters, except without redeposition (i.e. $\beta = 0$), is shown. Instead of ordered structures, spatio-temporally chaotic dynamics exhibit in the nonlinear regime of the surface evolution, which is the generic solution of the undamped Kuramoto-Sivashinsky equation [31].

The stabilization of patterns due to redeposition is quite a robust effect. This can be seen from Figure 16c, where we have used the chaotic surface from the bottom of the middle column as initial surface. Although a more complicated surface morphology is present in the upper picture of the right column now, redeposition is

[2] These parameters are exactly the same as in our letter [53], but here we discuss the results in more detail. Minor deviations in the results are the consequence of different random perturbations of the initially almost flat surface.

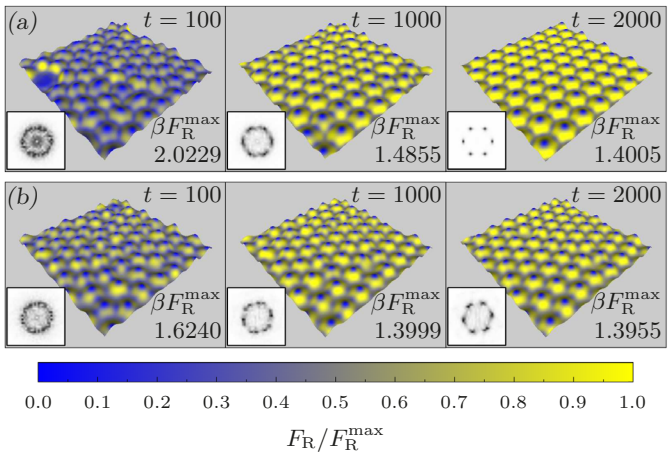

Fig. 17. (a) Evolution with Y_{const}, $f_{\cos\theta}$, $\beta = 5.5$ and $\kappa = -1.0$. (b) Evolution with the small-gradient approximation $F_{\text{R}} = F_{\text{R}}^{\text{B}}$, $\beta = 3.5$ and $\kappa = -1.0$.

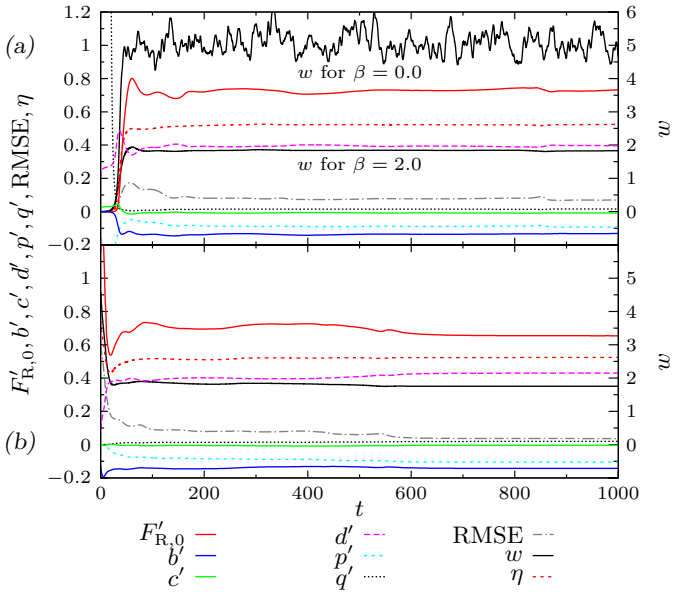

Fig. 18. (a) Temporal evolution of the fit coefficients for the simulation depicted in Figure 16a. Additional, the roughness w of Figure 16b is shown. (b) Coefficient curves for the evolution of Figure 16c.

again predominantly present at the slopes in the vicinity of the valleys, whereas almost no particles reattach at the top regions of the rugged ridges. During the spatio-temporal evolution of this initial surface, the rough morphology smoothens and hills emerge, which assemble again to a highly regular hexagonal dot pattern ($A = 6.18$ and $L = 8.71$). Thus, the interplay of erosion and redeposition is even able to create well-ordered structures starting with non-trivial and rough initial surfaces.

Moreover, it is not necessary to use the models Y_{tilt} and f_{skew}. As a representative example, we have depicted the surface evolution with the models Y_{const}, $f_{\cos\theta}$ and the parameters $\beta = 5.5$ and $\kappa = -1.0$ in Figure 17a. Again, the surface converges to a hexagonal arrangement of dot structures ($A = 4.66$, $L = 8.92$) and shows the typical redeposition distribution.

The pattern formation can also be observed when the full redeposition model F_{R} in the combined model equation (47) is replaced by the small-gradient approximation F_{R}^{B}. This is shown in Figure 17b, where we have used $\beta = 3.5$, $\kappa = -1.0$ and $JV_{\text{a}}Y(0) = 1$ and $f_{\varphi} = 1/\pi$ within F_{R}^{B}. We conclude that, even though redeposition sets in quadratically with increasing roughness on shallow surfaces, this non-local effect can have a robustly pattern-forming impact on the Kuramoto-Sivashinsky equation.

4.2 Approximation in terms of the surface height

In this section, we want to connect the spatio-temporal dynamics from the previous section to the approximation (33) discussed in Section 3.3. Since the amplitude A is hard to define on irregular surfaces, we will use the non-normalized ansatz (34). Moreover, we include the parameter β into the coefficients, i.e. we fit βF_{R} via

$$\begin{aligned}\beta F_{\text{R}} \approx \beta F_{\text{R}}^{\text{app.}} &= F'_{\text{R},0} + b'(H-\bar{H}) + c'(H-\bar{H})^2 \\ &+ (\nabla H)^2 \cdot \Big(d' + p'(H-\bar{H}) + q'(H-\bar{H})^2 \Big). \end{aligned} \quad (48)$$

By performing the fit procedure described in Section 3.3 in every time step, we are able to extract the temporal evolution of the fit coefficients. Based on the surface evolution of Figure 16a, we have depicted the corresponding coefficients in Figure 18a. For early times $t < 50$, the coefficients vary in time. The coefficients $F'_{\text{R},0}$, b' and c' are close to zero for the shallow surface and set in with increasing surface height modulations. The latter are measured here by the rms roughness w, which is also depicted in the graph. For comparison, also the roughness evolution of the spatio-temporal chaotic run of Figure 16b is shown. The coefficients p' and q' are subject to extreme changes during the initial transient time. This behavior can be attributed to the fact that F_{R} has a quadratic onset with increasing surface roughness, whereas the fit terms corresponding to these fit coefficients are functions of higher powers of $H - \bar{H}$. During the fit, the difference in the powers has to be compensated by p' and q', respectively. Although the surface is relatively flat at initial times, the fit error RMSE increases to its maximum in this regime. The fit $F_{\text{R}}^{\text{app.}}$ deviates here from F_{R} due to the irregularity of the surface. However, after the transient time, when the roughness begins to saturate and structures begin to arrange, all fit coefficients take on nearly constant values and RMSE decreases again.

We have depicted the curves corresponding to the simulation from Figure 16c in Figure 18b, where basically the same facts can be observed. The converged coefficients can be read off at $t = 1000$:

$$\begin{aligned} F'_{\text{R},0} &= 0.654, \quad & b' &= -0.143, \quad & c' &= -0.003, \\ d' &= 0.430, \quad & p' &= -0.105, \quad & q' &= 0.019. \end{aligned} \quad (49)$$

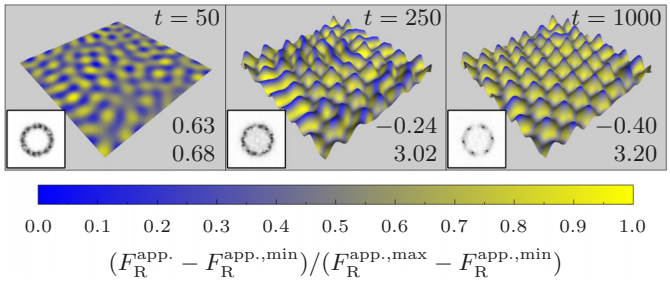

Fig. 19. Evolution of the approximative equation (52) with constant parameters according to (49). The values in the lower right of the pictures are $\beta F_R^{app.,min}$ and $\beta F_R^{app.,max}$, i.e. maximum and minimum of the color-coded approximated redeposition.

Using the relations

$$F'_{R,0} = \beta F_{R,0}, \quad b' = \beta\hat{b}/A, \quad c' = \beta\hat{c}/A^2,$$
$$d' = \beta d, \quad p' = \beta\hat{p}/A, \quad q' = \beta\hat{q}/A^2, \tag{50}$$

we can compare these with the ones stemming from the static analysis in Section 3. From corresponding data of Figure 11e, we can determine:

$$F'_{R,0} = 0.728, \quad b' = -0.129, \quad c' = -0.009,$$
$$d' = 0.413, \quad p' = -0.115, \quad q' = 0.023. \tag{51}$$

Thus, the static analysis of F_R can be used as a good estimation for the coefficients that are present in the spatio-temporal dynamic simulation after the transient time. Minor deviations between the results (50) and (51) can be ascribed to different lateral discretizations (cf. Appendix A). Furthermore, due to the presence of $\kappa(\nabla H)^2$ and F_R, the emerged hexagonal pattern does not need to exactly match the static prestructure (29).

The utility of the approximation $F_R \approx F_R^{app.}$ is elucidated by substituting it into the model equation (47), i.e.

$$\partial_t H = F'_{R,0} + b'\left(H-\bar{H}\right) + c'\left(H-\bar{H}\right)^2 + \left(d' + p'\left(H-\bar{H}\right) + q'\left(H-\bar{H}\right)^2\right)\cdot(\nabla H)^2 - \nabla^2 H - \nabla^4 H + \kappa\left(\nabla H\right)^2. \tag{52}$$

Accepting deviations in the transient regime at initial times, we can use the converged values (49) as constant coefficients. The resulting evolution is depicted in Figure 19. As expected, the approximative model (52) does not show exactly the same evolution as the full redeposition model (47), but the converged hexagonally arranged dot structures are comparable with respect to lateral and height extents. The redeposition approximation $F_R^{app.}$ shows a very similar distribution on the surface as the full model F_R. In the light of these results, the purpose of the approximation $F_R^{app.}$ is emphasized due to its ability to produce comparable results even in spatio-temporal dynamic simulations.

Of course, the incorporation of $F_R^{app.}$ into the model leads to a vast number of coefficients in combination with the Kuramoto-Sivashinsky equation by what it cannot be considered as minimal model anymore. However, the derivation of the Kuramoto-Sivashinsky equation as erosion model is typically achieved by a systematic expansion in terms compatible with the symmetries to the lowest order [22,38,59]. If $F_R^{app.}$ is truncated at the quadratic order in the height H, corresponding to the minimal $(\nabla H)^2$-term, one is left with the linearly and quadratically damped Kuramoto-Sivashinsky equation:

$$\partial_t H = F'_{R,0} + b'(H-\bar{H}) + c'(H-\bar{H})^2 - \nabla^2 H - \nabla^4 H + (d'+\kappa)\left(\nabla H\right)^2. \tag{53}$$

With a glance at the extracted coefficients (49), we notice that the quadratic damping term contributes only marginally to the evolution in this case. Moreover, as an important result, we conclude that $d' + \kappa > 0$, i.e. the $(\nabla H)^2$-term has positive sign. This fact clarifies an issue the damped KSE-model had to struggle with: while the pure erosive mechanism corresponding to this term – the enhanced sputter yield on slopes – necessitates a negative sign, the formation of hexagonal dot structures can only be found for positive coefficients. The extended interpretation of this term, now consisting of a negative contribution stemming from erosion ($\kappa < 0$) and a positive addend $d' > -\kappa$ caused by redeposition, is able to resolve this discrepancy. The simulation of (53) with the coefficients (49) leads to hexagonal dot structures, however, with an amplitude A exceeding the ones of Figures 16a and 16c or Figure 19 by one order of magnitude. Due to the small moduli of the coefficients c and $\kappa + d'$ and the neglection of the terms of higher order, the saturation sets in at later times and at a higher roughness. However, it is also questionable if it is sufficient to expand the erosion model only up to the quadratic order in H. In particular for structures with an aspect ratio of $\epsilon \approx 1$, terms of higher order could have a massive impact on the evolution. Keeping that in mind, the ability of (53) to produce hexagonal ordered dot patterns with the coefficients (49) by itself substantiates the model of the linearly (and quadratically) damped Kuramoto-Sivashinsky equation. We investigate a local variant of (53) in reference [43].

4.3 Parameter map

The representative discussion of single simulations of the full model (47) is definitely fruitful, but a systematic investigation of the model equation (47) has also to include the dependency of typical solutions on the parameters. This issue will be addressed this section. Due to the numerical effort for a single simulation (cf. Appendix A), we restrict our discussion here to Y_{tilt}, f_{skew} and the parameter regions $0 \leq \beta \leq 5$ and $-1 \leq \kappa \leq 1$. In a first step, slightly perturbed hexagonally arranged dot and hole structure according to (29) were used as initial surfaces for simulations of (47) with β and κ in the afore-mentioned range. This procedure gives insight into the stability of prestructured surfaces as function of the parameters. The second step involves the same parameter scan starting with a slightly

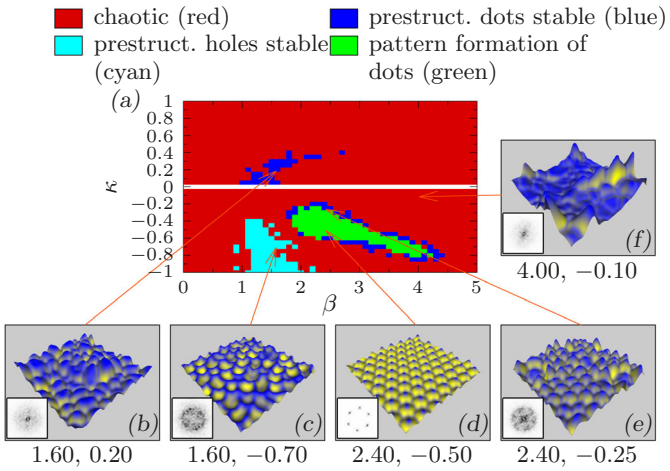

Fig. 20. Parameter map for Y_{tilt} and f_{skew} and some representative final surfaces evolved from a flat surface (captions are (β, κ)).

perturbed flat initial surface. Thereby, we were able to investigate for which (β, κ) self-organized pattern formation can be observed.

After a simulation time of $t = 1000$, we have determined the actual present final surface. The actual surface morphology was classified by a combination of several indicators: the evolution of the surface roughness $w(t)$ was checked for convergence. In the case of a non-trivial temporal behavior, we have also applied the 0-1-test for chaos [60] to distinguish between (quasi-)periodic and chaotic evolutions. Furthermore, the arrangement of the dominant modes in the PSD was investigated and, finally, we have connected the adjacent hilltops or valley centers by a net in the position space and analyzed its symmetry and regularity. In total, this method gives consistent results which coincide with a morphology classification made by eye.

The resulting parameter map is depicted in Figure 20a. Chaotic behavior can be found in large regions of the parameter space (red). Neither pattern formation can be observed within these areas, nor are there prestructured patterns stable. Besides the typical chaos of the undamped KSE, quite different chaotic solutions have been found. At $\beta = 4.0$ and $\kappa = -0.1$, for instance, isolated hogbacks can be observed (cf. Fig. 20f). Although a prestructured dot pattern is stable for the parameters of Figure 20b, a self-organized emergence of this structure cannot be found (indicated by blue regions in Fig. 20a). Similarly, the hole structures in Figure 20c do not assemble to a hexagonal formation, but a prestructured hole pattern is stable here (cyan regions).

Self-organized pattern formation can be observed in the green region. The corresponding patterns are all hexagonally arranged dot morphologies (cf. Fig. 20d) with aspect ratios ranging from $\epsilon = 0.51$ at $(\beta, \kappa) = (4.2, -0.8)$ to $\epsilon = 1.38$ at $(2.3, -0.3)$. The region of pattern formation is surrounded by a blue border in which only prestructured dot structures are stable. However, it can also be possible that the slightly hexagonal morphology in Figure 20e converges to a pattern for longer simulation times.

We can conclude by the extent of the green region of the parameter map that the pattern formation discussed in section 4.1 is a generic feature of the combined redeposition and erosion model (47). The resulting aspect ratios are in the same order as the experiments on binary compounds [6–11] and Ge irradiated by Bi-(cluster)-ions [12–17]. Additionally, the negative sign of κ is compatible with the physical interpretation of this parameter. However, we have not seen self-organized formation of hole patterns yet. This could be an effect of the limited redeposition range, which has been discussed in Section 3.6: the confinement of redeposition to each individual hole does not give rise to long-range interactions between the holes and could be the reason for the absence of a long-range ordering. However, an extension of the considered parameter range or a different choice for Y or f could also be able to give rise to the formation of well-arranged hole morphologies.

4.4 Combination with other erosion models

In a last step, we are interested if the pattern formation induced by redeposition can also be observed in combination with other erosion models. Recently, Bradley and Shipman proposed a erosion model (BS-model) for binary compounds, where the dynamics of the surface height H is coupled with a composition field ϕ [36,37]. Although this model is able to reproduce patterns without considering redeposition, we investigate briefly the influence of redeposition in this erosion model. For simplicity, we neglect the fact that the redepositing particles will also affect the composition field ϕ. The resulting combined model can be written as:

$$\partial_t \begin{pmatrix} H \\ \phi \end{pmatrix} = \begin{pmatrix} a_1\nabla^2 + a_2\nabla^4 & b \\ c\nabla^2 & d_0 + d_1\nabla^2 \end{pmatrix} \cdot \begin{pmatrix} H \\ \phi \end{pmatrix} + \begin{pmatrix} a_3\left(\nabla H\right)^2 + \beta F_{\text{R}} \\ d_2\phi^2 + d_3\phi^3 \end{pmatrix}. \tag{54}$$

Before concerning about the influence of redeposition in equation (54), we would like to discuss the pure erosion BS-model (i.e. $\beta = 0$): it is often stated that the pattern formation in this model is a result of the linear terms which can exhibit a finite wavelength bifurcation where only a small band of finite wave numbers are selected in the linear regime [36,37,51,61]. Although this fact distinguishes the BS-model from the chaotic undamped KSE, the BS-model also has a marginal stability in the limit of small wave numbers $k \to 0$. If the nonlinearities of the composition field are negligible, i.e. $d_2 = d_3 = 0$, the BS-model has much in common with a model for seismic waves proposed by Nikolaevskiy, namely a finite wavelength bifurcation in combination with a marginal stability for $k \to 0$ and a $(\nabla H)^2$-nonlinearity [62]. The Nikolaevskiy-model is known for showing so-called soft-mode turbulent

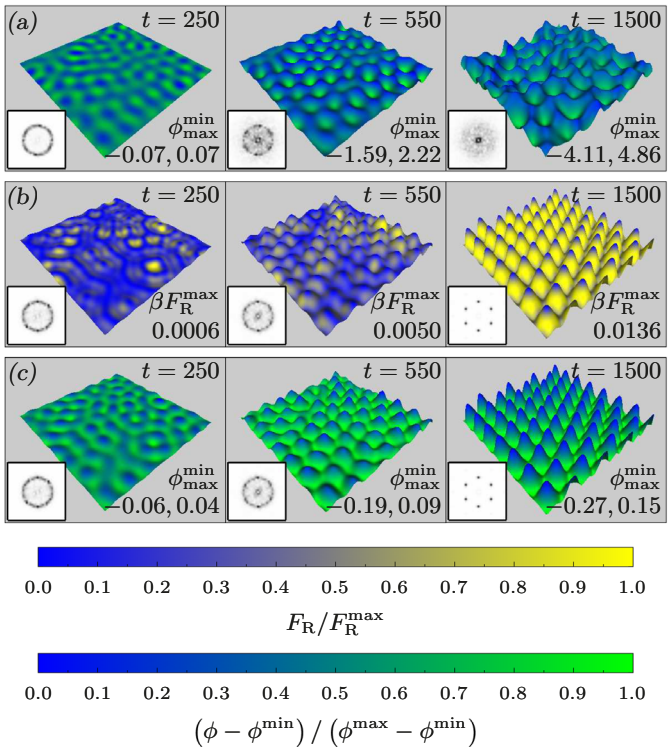

Fig. 21. (a) Soft-mode turbulence in the Bradley-Shipman model without composition nonlinearities. (b) The consideration of redeposition stabilizes patterns. (c) Same height as (b), but with color-coded composition field ϕ. For the sake of visibility, (b) and (c) are depicted with a height scale of 20, whereas (a) is true to scale.

chaotic behavior [63], which is also the generic solution of the BS-model without ϕ-nonlinearities.

A typical evolution of the latter with the coefficients

$$\begin{aligned} a_1 &= -1.00, \quad a_2 = -1.00, \quad a_3 = -0.10, \\ b &= 0.38, \quad c = 1.00, \quad d_2 = 0.00, \\ d_0 &= -0.25, \quad d_1 = 1.00, \quad d_3 = 0.00 \end{aligned} \tag{55}$$

is depicted in Figure 21a (height field H with color-coded composition field ϕ). A small band of finite wavelengths is selected in the linear regime ($t = 250$) and the corresponding modes even start to arrange towards a slightly hexagonal hole pattern ($t = 550$), but instead of converging to a perfect pattern, the order suddenly breaks up into a spatio-temporal chaotic dynamics ($t = 1500$). This soft-mode turbulence is a result of a complicated coupling between the $(\nabla H)^2$-nonlinearity and the marginal stability for long wavelengths.

By adding redeposition in this chaotic regime of the BS-model, we can investigate whether redeposition is able to stabilize the soft-mode turbulent behavior. Starting with the same initial condition as in Figure 21a, but including redeposition (Y_{tilt}, f_{skew} and $\beta = 3.0$), yields the result depicted in Figure 21b. One can see comparable surface evolution in the linear regime (see Fig. 21c for the same run as in Fig. 21b, but with the corresponding color-coded composition field ϕ). However, at $t = 550$, the presence of redeposition leads to the emergence of hill structures instead of the holes. In the limit of long times, redeposition prevents the soft-turbulence to break up the order and hexagonally arranged dots with the typical redeposition profile can be found. Interestingly, the resulting dot pattern (depicted with a height scale factor 20 in Figs. 21b and 21c) has an aspect ratio of only $\epsilon = 0.059$. Thus, although the redeposition effect is proportional to ϵ^2 here, it plays an decisive role for the resulting morphology.

Our conclusions regarding redeposition and the Bradley-Shipman model are twofold: on the one hand, we have found out that redeposition is also able to act as a stabilization mechanism when combined with other erosion models. On the other hand, the generic solution of the normal BS-model without ϕ-nonlinearities, Figure 21a, shows clearly that the pattern formation in the BS-model is not a direct result of the finite wavelength bifurcation. Instead, the composition nonlinearities $d_2\phi^2$ and/or $d_3\phi^3$ are additionally required prerequisites for pattern formation. The reproduction of the experimentally found nanopatterns within the framework of a continuum model can thus be done by two approaches: while the required symmetry $H \to H + \text{const.}$ do not allow for local absolute height terms, non-local height differences as in the redeposition model F_{R} or the non-locally damped KSE can be included to successfully reproduce the patterns. The patterns in a pure local model like the BS-model are not a direct consequence of the finite-wavelength bifurcation. Instead, by coupling in an additional field ϕ which is not restricted by a symmetry requirement $\phi \to \phi + \text{const.}$, absolute terms like ϕ^2 and ϕ^3 can be included. The latter stabilize the pattern by inhibiting the emergence of a soft-mode turbulence.

5 Conclusion

We have thoroughly investigated the impact of redepositing particles on the self-organized pattern formation during ion-beam erosion in the framework of a two-dimensional continuum model. The model exhibits a scale invariance with respect to an isotropic scaling of height and lateral extents of the surface. This simplifies the analysis, but also rules out a simple approximation of the redeposition function with constant coefficients. However, by analyzing static prestructured surface morphologies, we have shown that eroded particles predominantly redeposit in the vicinity of the valleys, whereas almost no particles reattach at the hilltops. This typical distribution is a characteristic property of the redeposition mechanism since it was found to be qualitatively independent of the specific models for the sputter yield, the angular erosion distribution and the considered surface morphology.

We were able to approximate the redeposition mechanism in terms of the relative height and the local slope, but the corresponding coefficients depend on the aspect ratio of the surface. This analysis – supported by the Fourier decomposition of the redeposition function – reveals a contribution in form of a linear damping term. Furthermore, higher order terms – in particular also the dependence on

the local slope – must also be taken into account. Thereby, a positive term $(\nabla H)^2$ arises due to the enhanced amount of redepositing particles when a surface element faces towards the neighboring structures.

Furthermore, we have investigated the origin of redepositing particles. The latter predominantly stem from erosion events within the range of the neighboring structures. Especially for hole patterns, redeposition is confined to each individual hole, whereas the distance between erosion and redeposition can be higher on hexagonally arranged dot morphologies.

After the investigation of prestructured surfaces, the spatio-temporal interplay of erosion and redeposition was analyzed. The combination of redeposition with the undamped Kuramoto-Sivashinsky equation as minimal erosion model can lead to an emergence of self-organized hexagonally ordered dot-structures. The latter have aspect ratios comparable with experiments and can be found in an extended region in the parameter space and even for non-trivial initial surfaces. Thus, redeposition can act as trigger for pattern formation under ion-beam erosion. While redeposition is not present for very flat surfaces, it sets in with increasing surface roughness and the corresponding fit coefficients of the afore-mentioned approximation converge quickly to constant values. In the nonlinear regime, both the full model and the approximation with the extracted coefficients support the arrangement of well-ordered dots with the typical redeposition profile.

Finally, we have briefly tested how redeposition interacts with the Bradley-Shipman erosion model for binary compounds. When the nonlinearities in the evolution equation for the composition field are neglected, the Bradley-Shipman model shows chaotic behavior (soft-mode turbulence). The influence of redeposition, however, is able to stabilize structures in combination with this erosion model as well, although redeposition is only marginally present for the resulting very shallow pattern.

The authors thank the Deutsche Forschungsgemeinschaft (FOR 845) for financial support.

Appendix A: Numerical algorithm

The numerical calculation of the redeposition functional F_R in two dimensions is only feasible when an elaborated algorithm is used. The implementation of our algorithm is briefly discussed in the following.

The height field is discretized on a cell-centered grid with $M \times N$ points and periodic boundary conditions. For each time-step and each of these points $\mathbf{x}_\mathrm{R}$, $F_\mathrm{R}(\mathbf{x}_\mathrm{R}, t)$ has to be calculated by integrating over all surrounding grid points $(\mathbf{x}_\mathrm{E}, H_\mathrm{E})$ that are visible from the considered position $(\mathbf{x}_\mathrm{R}, H_\mathrm{R})$. Due to the periodic boundaries, the range of the integral, i.e. of the possible visibility range, is not bounded. This can be clearly seen when a perfect ripple surface $H(x, y) = \cos(kx)$ is considered: the visibility v_H becomes a function of x_R and x_E only and if $v_H(x_\mathrm{R}, x_\mathrm{E}) = 1$ holds, visibility is given for all y_R and y_E, in particular for $|y_\mathrm{R} - y_\mathrm{E}| \to \infty$. Therefore, the integration range has to be restricted in the numerical algorithm to a finite distance R (measured in grid points) between $\mathbf{x}_\mathrm{R}$ and $\mathbf{x}_\mathrm{E}$. We will discuss an appropriate choice for R later on.

A straight-forward implementation of the visibility determination according to the definition (13) would have to evaluate $d_H(\mathbf{x}_\mathrm{R}, \mathbf{x}_\mathrm{E}, \mu)$ for all $\mu \in (0, 1)$. In total, this would lead to a calculation time of $\mathcal{O}(MNR^3)$ for one time-step, where the factors MN, R^2 and R stem from the iteration over all considered points $\mathbf{x}_\mathrm{R}$, the integration over all points $\mathbf{x}_\mathrm{E}$ within the range R and the determination of the visibility along the connection line, respectively.

In our algorithm, we exploit several properties of the visibility function: since $v_H(\mathbf{x}_1, \mathbf{x}_2)$ is symmetric with respect to its arguments, the visibility for each point $\mathbf{x}_1$ is only determined for all $\mathbf{x}_2$ in the upper semicircle with radius R (cf. Fig. A.1a). In case of visibility, the F_R-integral contributions with $\mathrm{both}(\mathbf{x}_\mathrm{R}, \mathbf{x}_\mathrm{E}) = (\mathbf{x}_1, \mathbf{x}_2)$ and $(\mathbf{x}_\mathrm{R}, \mathbf{x}_\mathrm{E}) = (\mathbf{x}_2, \mathbf{x}_1)$ are accumulated simultaneously to the corresponding result $F_\mathrm{R}(\mathbf{x}_\mathrm{R})$. Furthermore, for each $\mathbf{x}_1$, the visibility of all points $\mathbf{x}_2$ which are laterally located on the same line are calculated in a single pass. Thereby, each of these lines is reduced to a one-dimensional visibility determination. For each of these lines, all lateral intersection points with the grid are calculated in beforehand (Fig. A.1b). To that end, each grid cell is decomposed into four triangles with intermediate corner points interpolated at quadratic order. The lateral coordinates of the intersection points are calculated only once for a single $\mathbf{x}_1$ since the same stencil applies for the entire grid. In order to circumvent range overflow tests, the grid is periodically extended by R points into all four directions in beforehand, but the iteration over all $\mathbf{x}_1$ only comprises the central $M \times N$ points. Since F_R-integral contributions stemming from the symmetric visibility accumulation at $\mathbf{x}_2$ can be outside this area, these contributions are additively mapped to the corresponding central points at the end of each algorithm pass. Furthermore, a field H^max of the size $M \times N$ is initialized, which stores the maximum height for each grid point and the corresponding adjacent interpolated intermediated points.

The one-dimensional visibility determination along all points $\mathbf{x}_2$ which lie on the same line is illustrated in Figure A.1c: we introduce the lateral coordinate λ along the line starting with $\lambda = 0$ at $\mathbf{x}_1$ and having each grid point $\mathbf{x}_2$ located at the integers $\lambda = 1, 2, \ldots$ The visibility determination begins with a ray starting at $(\lambda = 0, H(\mathbf{x}_1))$ and with a slope that is initialized by the directional derivative of the surface height along the line direction. Every point $(\lambda, H(\mathbf{x}_2(\lambda)))$ at $\lambda = 1, 2, \ldots$ that is below this ray cannot be visible from the considered starting point. If however the height at a grid point $\mathbf{x}_2$ is above the ray, visibility cannot be ruled out. Next, the directional derivative at these $\mathbf{x}_2$ is compared with the current ray slope, by what e.g. the point at $\lambda = 1$ in Figure A.1c can be marked as invisible. The ray slope is increased to match the connecting line from $\lambda = 0$ to $\lambda = 1$ since all following points with $\lambda > 1$ will be obstructed when they are below this

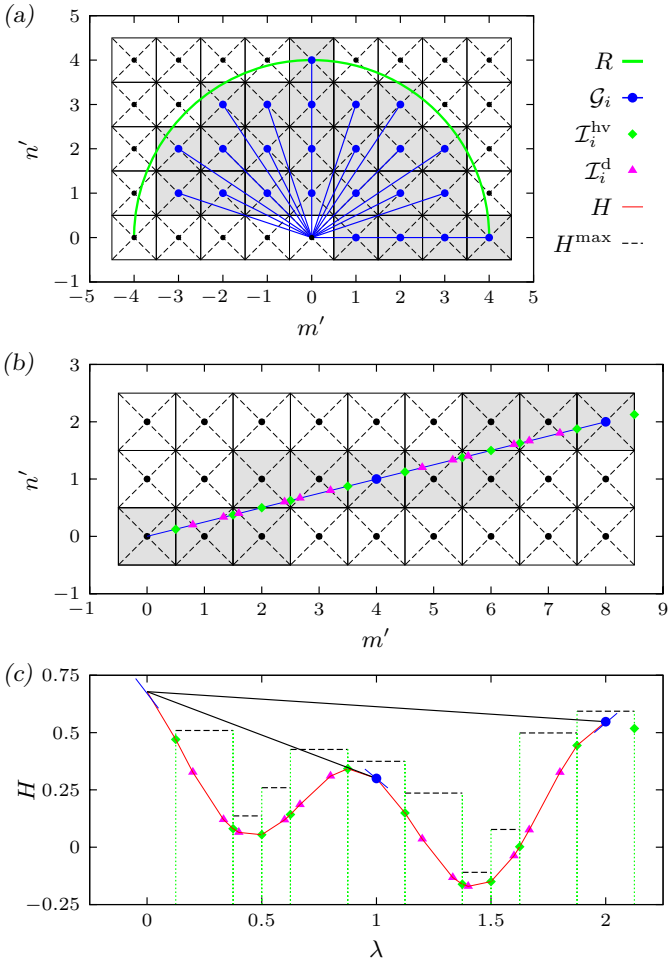

Fig. A.1. Schematic illustration of the algorithm: (a) before the algorithm starts, a stencil is build by grouping all points within the range $m'^2 + n'^2 \leq R^2$ into line groups $\mathcal{G}_i$ ($i = 1, 2, \ldots$). (b) For each line $\mathcal{G}_i$, all corresponding lateral intersection coordinates $\mathcal{I}_i^{\mathrm{hv}}$ and $\mathcal{I}_i^{\mathrm{d}}$ with the horizontal and vertical and with the diagonal grid partition, respectively, are calculated. (c) One-dimensional algorithm along each of the line groups from (a) using the calculated lateral intersection data from (b).

new ray. The point at $\lambda = 2$ in Figure A.1c, however, cannot be ruled out as invisible by the mentioned criteria because it is located above the current ray and the surface element faces towards starting point. In this case, the algorithm has to investigate the surface height on a finer level. This is accomplished by comparing the height along the ray with the maximum values stored in $H^{\max}$ (bars in Fig. A.1c). Only when the ray is beneath the corresponding height $H^{\max}$, the finest level – i.e the height at the intersection points $\mathcal{I}_i^{\mathrm{d}}$ in Figures A.1b and A.1c – has to be investigated. Thus, there are three levels of detail in the algorithm, where the next finer level is only investigated when the visibility cannot be determined at the current level. A final optimization is achieved by testing the ray height against the global maximum of the surface. The current one-dimensional pass can be terminated when the ray with a positive slope exceeds this height, because all following points will be obstructed.

The spatio-temporal integration of the evolution equations (47), (52)–(54) is implemented based on a pseudo-spectral method [64] in combination with an exponential time-differencing scheme [65].

Used discretizations

The algorithm was validated based on the connection to the one-dimensional redeposition model (cf. Sect. 2.4) and the corresponding solutions from reference [52]. For the static investigation of F_{R} on hexagonally arranged surfaces, we have used the discretization

$$M \times N = 84 \times 97, \quad \Delta x = \frac{2L}{97}, \\ R = 500 \text{ grid points}, \tag{A.1}$$

by what the error on the periodic boundary is minimized and more than ten lateral periods L are considered for the visibility determination. Since this discretization is not feasible to comprise multiple periods of self-organizing structures in each time-step of a spatio-temporal evolution, we have used

$$M \times N = 100 \times 100, \quad \Delta x = 0.71086127, \\ R = 40 \text{ grid points}, \tag{A.2}$$

in Section 4 (except $\Delta x = 0.820832$ in Fig. 21). With these parameters, 8×7 hexagonally arranged structures with the critical wavenumber k_{c} fit into the grid. However, in comparison to the fine discretization (A.1), there are now only approximately 14.43 instead of 48.5 grid points per characteristic length L. To investigate the error stemming from a coarser discretization, we have prestructured hexagonal dot structures with $L = 1$ on a 84×97 grid, but with different discretizations Δx. The integration radius R was scaled appropriately in order to consider always the same number of lateral periods. From the results in Figures A.2a and A.2b it is apparent that a coarser discretization has only a minor impact on the calculated redeposition F_{R}. The discretization in Figure A.2b samples a lateral period L with 12.125 grid points. Thus, the parameters (A.2) used for the spatio-temporal evolution is even more accurate than Figure A.2b.

Furthermore, the integration range $R = 40$ from the parameters (A.2) comprises now only approximately three lateral periods L instead of more than ten period in (A.1), but from Figure 14 it can be inferred that the relevant part of F_{R} is included within this range. To substantiate this specific choice of R, we have investigated the impact of R for representative time-steps of the evolutions depicted in Figures 16a and 16c. We have chosen the redeposition ratio η as indicating quantity since it is a direct measure of the considered redepositing particles. From the graphs in Figure A.2c it is apparent that at $R = 40$ almost the entire amount of redepositing particles has been considered. The maximum deviation between η at $R = 40$ and the

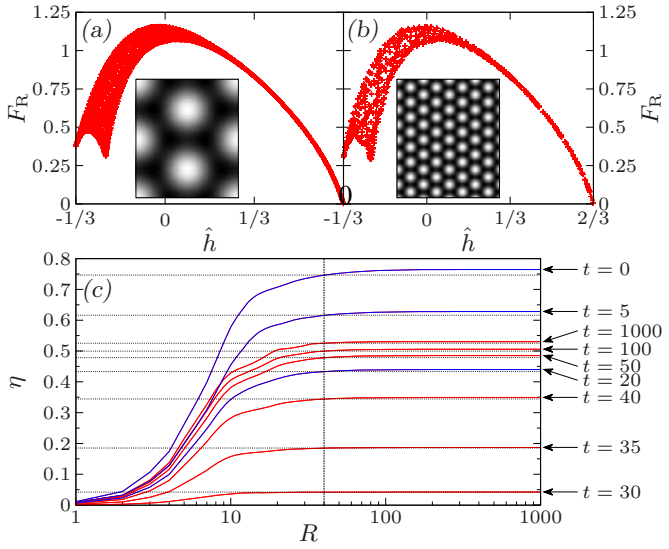

Fig. A.2. (a,b) F_R plotted against $\hat{h}$ for different spatial discretizations Δx: (a) $\Delta x = 2/97$ and $R = 720$ grid points, (b) $\Delta x = 8/97$ and $R = 180$ grid points. (c) Influence of the considered integration radius R on the redeposition ratio η for individual time-steps from the evolution depicted in Figure 16a (red) and Figure 16c (blue).

converged value at $R = 1000$ is below 2.5%. Hence, the relevant part of redeposition is considered with a maximum visibility radius of $R = 40$.

Appendix B: Fit coefficients for the small-gradient approximation F_R^B

For the small-gradient approximation F_R^B (cf. Eq. (20)) we have determined the fit coefficients of (33) by the procedure described in Section 3.3. With the appropriate value $f_\theta = 1/\pi$, the quadratic onsets of the fit coefficients for $\epsilon \approx 0$ coincide with the corresponding curves for $f_{\cos\theta}$ and f_{skew}.

For the case $Y = Y_{\text{const}}$, the coefficients for F_R^B read for hexagonally ordered dot structures (with $JV_aY(0) = 1$):

$$\begin{aligned} F_{R,0} &= 0.887{\cdot}\epsilon^2, & \hat{b} &= -1.793{\cdot}\epsilon^2, & \hat{c} &= 0.684{\cdot}\epsilon^2, \\ d &= 0.265, & \hat{p} &= -0.073, & \hat{q} &= 0.027, \\ & & \text{RMSE} &= 0.004{\cdot}\epsilon^2, \end{aligned} \tag{B.1}$$

whereas the following results were obtained on the nanohole morphology:

$$\begin{aligned} F_{R,0} &= 0.463{\cdot}\epsilon^2, & \hat{b} &= -2.785{\cdot}\epsilon^2, & \hat{c} &= 4.165{\cdot}\epsilon^2, \\ d &= 0.294, & \hat{p} &= -0.100, & \hat{q} &= -0.061, \\ & & \text{RMSE} &= 0.003{\cdot}\epsilon^2. \end{aligned} \tag{B.2}$$

The Fourier coefficients $\tilde{F}_i$, which have been discussed in Section 3.4, have the following numerical values for dots:

$$\begin{aligned} \tilde{F}_0 &= 1.947{\cdot}\epsilon^2, & \tilde{F}_1 &= -0.065{\cdot}\epsilon^2, & \tilde{F}_2 &= -0.317{\cdot}\epsilon^2, \\ \tilde{F}_3 &= -0.309{\cdot}\epsilon^2, & \tilde{F}_4 &= 0.006{\cdot}\epsilon^2, & \tilde{F}_5 &= 0.020{\cdot}\epsilon^2, \\ & & \text{RMSE} &= 0.004{\cdot}\epsilon^2 \end{aligned} \tag{B.3}$$

while on holes the corresponding values are

$$\begin{aligned} \tilde{F}_0 &= 1.946{\cdot}\epsilon^2, & \tilde{F}_1 &= 1.265{\cdot}\epsilon^2, & \tilde{F}_2 &= -0.293{\cdot}\epsilon^2, \\ \tilde{F}_3 &= -0.180{\cdot}\epsilon^2, & \tilde{F}_4 &= -0.008{\cdot}\epsilon^2, & \tilde{F}_5 &= -0.025{\cdot}\epsilon^2, \\ & & \text{RMSE} &= 0.007{\cdot}\epsilon^2. \end{aligned} \tag{B.4}$$

References

1. J. Muñoz-García, L. Vázquez, R. Cuerno, J. Sánchez-García, M. Castro, R. Gago, in *Toward Functional Nanomaterials*, Lecture Notes in Nanoscale Science and Technology, edited by Z.M. Wang (Springer-Verlag New York, 2009), Vol. 5, pp. 323–398
2. G. Carter, J. Phys. D **34**, R1 (2001)
3. W.L. Chan, E. Chason, J. Appl. Phys. **101**, 121301 (2007)
4. J. Muñoz-García, L. Vázquez, M. Castro, R. Gago, A. Redondo-Cubero, A. Moreno-Barrado, R. Cuerno, Mater. Sci. Eng. R **86**, 1 (2014)
5. M. Navez, C. Sella, D. Chaperot, C.R. Hebd. Acad. Sci. **254**, 240 (1962)
6. S. Facsko, T. Dekorsy, C. Koerdt, C. Trappe, H. Kurz, A. Vogt, H.L. Hartnagel, Science **285**, 1551 (1999)
7. F. Frost, A. Schindler, F. Bigl, Phys. Rev. Lett. **85**, 4116 (2000)
8. S. Facsko, T. Bobek, T. Dekorsy, H. Kurz, Phys. Stat. Sol. B **224**, 537 (2001)
9. S. Facsko, H. Kurz, T. Dekorsy, Phys. Rev. B **63**, 165329 (2001)
10. F. Frost, B. Rauschenbach, Appl. Phys. A **77**, 1 (2003)
11. F. Frost, B. Ziberi, T. Höche, B. Rauschenbach, Nucl. Instrum. Meth. B **216**, 9 (2004)
12. L. Bischoff, W. Pilz, B. Schmidt, Appl. Phys. A **104**, 1153 (2011)
13. L. Bischoff, K.H. Heinig, B. Schmidt, S. Facsko, W. Pilz, Nucl. Instrum. Meth. B **272**, 198 (2012)
14. R. Böttger, L. Bischoff, S. Facsko, B. Schmidt, Europhys. Lett. **98**, 16009 (2012)
15. R. Böttger, L. Bischoff, K.H. Heinig, W. Pilz, B. Schmidt, J. Vac. Sci. Technol. B **30**, 06FF12 (2012)
16. R. Böttger, K.H. Heinig, L. Bischoff, B. Liedke, S. Facsko, Appl. Phys. A **113**, 53 (2013)
17. R. Böttger, K.H. Heinig, L. Bischoff, B. Liedke, R. Hübner, W. Pilz, Phys. Stat. Sol. RRL **7**, 501 (2013)
18. G. Ozaydin, A.S. Özcan, Y. Wang, K.F. Ludwig, H. Zhou, R.L. Headrick, D.P. Siddons, Appl. Phys. Lett. **87**, 163104 (2005)
19. G. Ozaydin, K.F. Ludwig, H. Zhou, R.L. Headrick, J. Vac. Sci. Technol. B **26**, 551 (2008)
20. J.A. Sánchez-García, L. Vázquez, R. Gago, A. Redondo-Cubero, J.M. Albella, Z. Czigány, Nanotechnology **19**, 355306 (2008)

21. J. Zhou, S. Facsko, M. Lu, W. Möller, J. Appl. Phys. **109**, 104315 (2011)
22. R. Cuerno, A.L. Barabási, Phys. Rev. Lett. **74**, 4746 (1995)
23. W.W. Mullins, J. Appl. Phys. **28**, 333 (1957)
24. G. Carter, V. Vishnyakov, Phys. Rev. B **54**, 17647 (1996)
25. R.M. Bradley, J.M.E. Harper, J. Vac. Sci. Technol. A **6**, 2390 (1988)
26. S.A. Norris, J. Appl. Phys. **114**, 204303 (2013)
27. M. Raible, S. Linz, P. Hänggi, Eur. Phys. J. B **27**, 435 (2002)
28. M. Raible, S.J. Linz, P. Hänggi, Phys. Rev. E **64**, 031506 (2001)
29. M. Raible, S.J. Linz, P. Hänggi, Phys. Rev. E **62**, 1691 (2000)
30. J.M. Hyman, B. Nicolaenko, S. Zaleski, Physica D **23**, 265 (1986)
31. B.M. Boghosian, C.C. Chow, T. Hwa, Phys. Rev. Lett. **83**, 5262 (1999)
32. T. Bobek, S. Facsko, H. Kurz, T. Dekorsy, M. Xu, C. Teichert, Phys. Rev. B **68**, 085324 (2003)
33. S. Facsko, T. Bobek, A. Stahl, H. Kurz, T. Dekorsy, Phys. Rev. B **69**, 153412 (2004)
34. M. Castro, R. Cuerno, L. Vázquez, R. Gago, Phys. Rev. Lett. **94**, 016102 (2005)
35. C.S. Madi, B. Davidovitch, H.B. George, S.A. Norris, M.P. Brenner, M.J. Aziz, Phys. Rev. Lett. **101**, 246102 (2008)
36. R.M. Bradley, P.D. Shipman, Phys. Rev. Lett. **105**, 145501 (2010)
37. P.D. Shipman, R.M. Bradley, Phys. Rev. B **84**, 085420 (2011)
38. S. Vogel, S.J. Linz, Phys. Rev. B **72**, 035416 (2005)
39. S. Vogel, S.J. Linz, Europhys. Lett. **76**, 884 (2006)
40. S. Vogel, S.J. Linz, Phys. Rev. B **75**, 085425 (2007)
41. S. Vogel, S.J. Linz, Phys. Rev. B **75**, 155417 (2007)
42. K. Dreimann, S.J. Linz, Chem. Phys. **375**, 606 (2010)
43. M. Osthues, C. Diddens, S.J. Linz, in preparation
44. R. Smith, S.S. Makh, J.M. Walls, Philos. Mag. B **47**, 453 (1983)
45. R. Smith, M. Tagg, J. Walls, Vacuum **34**, 175 (1984)
46. H.B. Kim, G. Hobler, A. Steiger, A. Lugstein, E. Bertagnolli, Nanotechnology **18**, 265307 (2007)
47. J. Saussac, J. Margot, L. Stafford, M. Chaker, J. Appl. Phys. **107**, 063306 (2010)
48. S. Lindsey, G. Hobler, Nucl. Instrum. Meth. B **282**, 12 (2012)
49. N. Anspach, S.J. Linz, J. Stat. Mech. **2010**, P06023 (2010)
50. N. Anspach, S.J. Linz, J. Stat. Mech. **2012**, P06012 (2012)
51. R.M. Bradley, Phys. Rev. B **83**, 075404 (2011)
52. C. Diddens, S.J. Linz, Eur. Phys. J. B **86**, 397 (2013)
53. C. Diddens, S.J. Linz, Europhys. Lett. **104**, 17010 (2013)
54. Q. Wei, K.D. Li, J. Lian, L. Wang, J. Phys. D **41**, 172002 (2008)
55. T. Chini, S. Bhattacharyya, D. Ghose, D. Basu, Nucl. Instrum. Meth. B **72**, 355 (1992)
56. H. Gnaser, *Low-energy Ion Irradiation of Solid Surfaces* (Springer, Berlin, 1999)
57. T. Chini, M. Tanemura, F. Okuyama, Nucl. Instrum. Meth. B **119**, 387 (1996)
58. T.J. Whitaker, P.L. Jones, A. Li, R.O. Watts, Rev. Sci. Instrum. **64**, 452 (1993)
59. M.A. Makeev, R. Cuerno, A.L. Barabási, Nucl. Instrum. Meth. B **197**, 185 (2002)
60. G.A. Gottwald, I. Melbourne, Proc. R. Soc. London A **460**, 603 (2004)
61. R.M. Bradley, P.D. Shipman, Appl. Surf. Sci. **258**, 4161 (2012)
62. I. Beresnev, V. Nikolaevskiy, Physica D **66**, 1 (1993)
63. H.W. Xi, R. Toral, J.D. Gunton, M.I. Tribelsky, Phys. Rev. E **62**, R17 (2000)
64. B. Fornberg, A Practical Guide to Pseudospectral Methods, *Cambridge Monographs on Applied and Computational Mathematics* (Cambridge University Press, 1996)
65. G. Beylkin, J.M. Keiser, L. Vozovoi, J. Comput. Phys. **147**, 362 (1998)